



NAVAL POSTGRADUATE SCHOOL

MONTEREY, CALIFORNIA

THESIS

ACTIVE VIBRATION CONTROL FOR FREE ELECTRON LASERS

by

Aaron M. Stetler

December 2003

Thesis Advisor:
Thesis Co-Advisor:

Bruce C. Denardo
Thomas J. Hofler

Approved for public release; distribution is unlimited

THIS PAGE INTENTIONALLY LEFT BLANK

REPORT DOCUMENTATION PAGE			Form Approved OMB No. 0704-0188	
Public reporting burden for this collection of information is estimated to average 1 hour per response, including the time for reviewing instruction, searching existing data sources, gathering and maintaining the data needed, and completing and reviewing the collection of information. Send comments regarding this burden estimate or any other aspect of this collection of information, including suggestions for reducing this burden, to Washington headquarters Services, Directorate for Information Operations and Reports, 1215 Jefferson Davis Highway, Suite 1204, Arlington, VA 22202-4302, and to the Office of Management and Budget, Paperwork Reduction Project (0704-0188) Washington DC 20503.				
1. AGENCY USE ONLY (Leave blank)		2. REPORT DATE December 2003	3. REPORT TYPE AND DATES COVERED Master's Thesis	
4. TITLE AND SUBTITLE: Active Vibration Control for Free Electron Lasers			5. FUNDING NUMBERS	
6. AUTHOR(S) Stetler, Aaron M.				
7. PERFORMING ORGANIZATION NAME(S) AND ADDRESS(ES) Naval Postgraduate School Monterey, CA 93943-5000			8. PERFORMING ORGANIZATION REPORT NUMBER	
9. SPONSORING /MONITORING AGENCY NAME(S) AND ADDRESS(ES) N/A			10. SPONSORING/MONITORING AGENCY REPORT NUMBER	
11. SUPPLEMENTARY NOTES The views expressed in this thesis are those of the author and do not reflect the official policy or position of the Department of Defense or the U.S. Government.				
12a. DISTRIBUTION / AVAILABILITY STATEMENT Approved for public release; distribution is unlimited			12b. DISTRIBUTION CODE	
13. ABSTRACT (maximum 200 words) <p>This thesis is concerned with active control methods for stabilizing the mirror vibrations of free-electron laser weapons on ships so that the laser continues to deliver full power. Alignment of the mirrors is critical for proper operation because the electron beam and optical mode must substantially overlap. The alignment is expected to be difficult to maintain in a shipboard environment. A theory for controlling the vibrations of a single-degree-of-freedom system is developed and checked by numerical simulations. An apparatus consisting of a flexing aluminum strip was constructed in order to probe the fundamental behavior of actual systems which eventually become unstable as the control gains are increased. A computer data acquisition system (LabVIEW) was implemented so that experiments could be more efficiently and accurately performed. Proportional and derivative controls were used to stabilize the motion of the strip. Experiments reveal that the derivative control behaves according to the theory. In particular, the instability is understood as the result of positive feedback due to a phase shift of the unstable mode. However, the instability due to the proportional control does not behave according to the theory. Improvements that would allow for greater control gains and thus greater stabilization are suggested.</p>				
14. SUBJECT TERMS Free-electron lasers, Active control, Vibration stabilization			15. NUMBER OF PAGES 103	
			16. PRICE CODE	
17. SECURITY CLASSIFICATION OF REPORT Unclassified	18. SECURITY CLASSIFICATION OF THIS PAGE Unclassified	19. SECURITY CLASSIFICATION OF ABSTRACT Unclassified	20. LIMITATION OF ABSTRACT UL	

NSN 7540-01-280-5500

Standard Form 298 (Rev. 2-89)
Prescribed by ANSI Std. Z39-18

THIS PAGE INTENTIONALLY LEFT BLANK

Approved for public release; distribution is unlimited

ACTIVE VIBRATION CONTROL FOR FREE ELECTRON LASERS

Aaron M. Stetler
Lieutenant, United States Navy
B.S., Purdue University, 1996

Submitted in partial fulfillment of the
requirements for the degree of

MASTER OF SCIENCE IN APPLIED PHYSICS

from the

**NAVAL POSTGRADUATE SCHOOL
December 2003**

Author: Aaron M. Stetler

Approved by: Bruce C. Denardo
Thesis Advisor

Thomas J. Hofler
Thesis Co-Advisor

James H. Luscombe
Chairman, Department of Physics

THIS PAGE INTENTIONALLY LEFT BLANK

ABSTRACT

This thesis is concerned with active control methods for stabilizing the mirror vibrations of free-electron laser weapons on ships so that the laser continues to deliver full power. Alignment of the mirrors is critical for proper operation because the electron beam and optical mode must substantially overlap. The alignment is expected to be difficult to maintain in a shipboard environment. A theory for controlling the vibrations of a single-degree-of-freedom system is developed and checked by numerical simulations. An apparatus consisting of a flexing aluminum strip was constructed in order to probe the fundamental behavior of actual systems which eventually become unstable as the control gains are increased. A computer data acquisition system (LabVIEW) was implemented so that experiments could be more efficiently and accurately performed. Proportional and derivative controls were used to stabilize the motion of the strip. Experiments reveal that the derivative control behaves according to the theory. In particular, the instability is understood as the result of positive feedback due to a phase shift of the unstable mode. However, the instability due to the proportional control does not behave according to the theory. Improvements that would allow for greater control gains and thus greater stabilization are suggested.

THIS PAGE INTENTIONALLY LEFT BLANK

TABLE OF CONTENTS

I.	INTRODUCTION.....	1
A.	BASIC FEL PRINCIPLES.....	2
B.	SHIPBOARD INTEGRATION ISSUES AND SPECIFICATIONS	4
C.	THESIS OBJECTIVES	5
II.	THEORY	7
A.	MODEL SYSTEM.....	7
B.	CONTROL AND STABILITY	9
C.	GANGING OF THE GAINS	11
III.	NUMERICAL SIMULATIONS.....	15
A.	DAMPED NOISE-DRIVEN OSCILLATOR.....	15
B.	PROPORTIONAL (STIFFNESS) CONTROL	20
C.	DERIVATIVE (RESISTIVE) CONTROL.....	23
D.	PROPORTIONAL-DERIVATIVE (PD) CONTROL.....	25
IV.	LABVIEW IMPLEMENTATION	31
A.	DAQ INPUT SAMPLING RATE	32
B.	DAQ OUTPUT SAMPLING RATE	34
C.	DAQ RESOLUTION	36
D.	DAQ LOOP RATE	38
E.	SERIES LC RESONANT CIRCUIT SIMULATION.....	40
V.	ACTIVE VIBRATION CONTROL EXPERIMENTS.....	47
A.	APPARATUS.....	47
B.	RESULTS.....	53
1.	Proportional Control.....	55
2.	Derivative Control	60
VI.	CONCLUSIONS & FUTURE WORK.....	65
A.	CONCLUSIONS	65

B.	FUTURE WORK.....	66
APPENDIX A	COMPUTER PROGRAM FOR NUMERICAL SIMULATIONS .	69
APPENDIX B	BASIC LABVIEW STARTUP STEPS.....	73
APPENDIX C	MOREL MW-113 LOUDSPEAKER SPECIFICATIONS.....	79
	LIST OF REFERENCES.....	81
	INITIAL DISTRIBUTION LIST	83

LIST OF FIGURES

Figure 1.	Basic FEL Schematic	2
Figure 2.	Basic FEL Operation	2
Figure 3.	Model of a Stable Two-Mirror Resonator	3
Figure 4.	Optical Mode Translation.....	3
Figure 5.	Model system with one translational degree of freedom.....	9
Figure 6.	Displacement amplitude for an oscillator driven by white noise, for different values of the feedback control proportional gain α and derivative gain β	13
Figure 7.	(a) Fast Fourier transform (FFT) of numerical random noise with time step 0.01. (b) Data from (a) smoothed over 20 adjacent points.	18
Figure 8.	(a) FFT of the position $x(t)$ of an oscillator driven by random noise. (b) Data from (a) smoothed over 20 adjacent points	19
Figure 9.	FFT's for different values of the proportional control gain α (or "xgain" in the computer program and in the above graphs).....	22
Figure 10.	FFT's for different values of the derivative control gain β (or "vgain" in the computer program and in the graphs above).....	24
Figure 11.	FFT's for different values of the proportional control gain α (xgain) for fixed derivative control gain β (vgain).....	28
Figure 12.	FFT's for different values of the proportional control gain α (xgain) and for corresponding values of the derivative control gain β (vgain) such that the motion is effectively critically damped in each case	29
Figure 13.	FFT's for different values of the control gains, which are large in (c) and (d).....	30
Figure 14.	'1 Channel Simple Scope.vi' Front Panel.....	33
Figure 15.	'1 Channel Simple Scope.vi' Block Diagram	33
Figure 16.	'Benchtop Function Generator.vi' Front Panel	35
Figure 17.	'Benchtop Function Generator.vi' Block Diagram	35
Figure 18.	Voltage divider circuit for DAQ resolution testing	36

Figure 19.	'Single Point Voltage Measurement.vi' Front Panel	37
Figure 20.	'Single Point Voltage Measurement.vi' Block Diagram	37
Figure 21.	'Real Time PID Control.vi' Front Panel	39
Figure 22.	'Real Time PID Control.vi' Block Diagram	39
Figure 23.	LabVIEW PD Controller Front Panel	41
Figure 24.	LabVIEW PD Controller Block Diagram.....	41
Figure 25.	Electrical equivalent circuit of physical model system	42
Figure 26.	Series LC resonator frequency response	43
Figure 27.	Plots of increasing proportional gain.....	44
Figure 28.	Plots of increasing derivative gain	45
Figure 29.	Diagram of experimental apparatus.....	48
Figure 30.	PSD ambient light response	49
Figure 31.	Loudspeaker Mounting and sample vibrating strip	51
Figure 32.	Driver Cup	52
Figure 33.	Sketch of mechanical bonding of loudspeaker and driver cup.....	52
Figure 34.	Frequency response of physical model system.....	53
Figure 35.	Proportional (α) Gain Only.....	55
Figure 36.	Effects of increased proportional gain on the first mode.....	57
Figure 37.	Effects of increased proportional gain on the third mode.....	58
Figure 38.	Effects of increased proportional gain on the fifth mode.....	59
Figure 39.	Derivative (β) gain only	60
Figure 40.	Effects of increased derivative gain on the first mode	62
Figure 41.	Effects of increased derivative gain on the third mode	63
Figure 42.	Effects of increased derivative gain on the fifth mode	64
Figure 43.	Desktop following login.....	73
Figure 44.	Selection of the execution target	75
Figure 45.	Selection of the VI to open	75
Figure 46.	Selection of 'pd.vi' as the controller	76
Figure 47.	Running the VI.....	76
Figure 48.	Parameters on the controller and halting execution	77

LIST OF TABLES

Table 1.	Theoretical and experimental modes of the vibrating strip	54
----------	---	----

THIS PAGE INTENTIONALLY LEFT BLANK

LIST OF SYMBOLS

α	Proportional gain
A	Amplitude
β	Derivative gain
C	Capacitor
c	damping coefficient
Δt	Time step
F	External force
f	External force per unit mass
f_0	Natural frequency
f_c	Cutoff frequency
G	Control Force
g	Control force per unit mass
Γ	Effective damping parameter
γ	Damping parameter
k	Spring constant
L	Inductor
m	Mass
ϕ	Phase
Π	Pi
Q	Quality factor
R	Resistor

t	Time
V	Voltage
x	Mass displacement
\dot{x}	One time derivative of x , velocity
\ddot{x}	Two time derivatives of x , acceleration
Ω	Effective natural angular frequency
ω	Angular frequency
ω_0	Natural angular frequency

LIST OF ACRONYMS

DAQ	Data Acquisition
FFT	Fast Fourier Transform
FEL	Free Electron Laser
LC	Inductor and Capacitor
LabVIEW	Laboratory Virtual Instrument Engineering Workbench
MIL-STD	Military Standard
NI	National Instruments
OPAMP	Operational Amplifier
OPNAV	Office of the Chief of Naval Operations
PD	Proportional-Derivative control
PID	Proportional-Derivative-Integral control
PSD	Position Sensitive Detector
PZT	Piezoelectric actuator (Plumbum Zirconate Titanate)
Q	Quality Factor
VI	Virtual Instrument

THIS PAGE INTENTIONALLY LEFT BLANK

ACKNOWLEDGMENTS

I would like to thank my close knit family and friends that have stood by me as I have moved forward through my Naval career. Without their unending support I would not have found the comfort in many of the places I have been or the places I am sure to go.

I would also like to extend many thanks to Professor Bruce Denardo for both his attention grabbing courses with visible demonstrations and all the time and patience he has afforded me as my advisor during this research. Thanks also go to my co-advisor Professor Tom Hofler for providing valuable insight into some of our design tasks and providing a fresh mind that helped us see clear through many of the physical system design and assembly challenges.

Thanks are also in order for the technical support lent to this research both from within the Naval Postgraduate School as well as from outside. Without the machining experience and know how of George Jaksha the physical model may never have come to being. This research entered a new dimension by incorporating LabVIEW 7 as the controller. Many hours of work went into both choosing the data acquisition components and developing the code required for the controller in the research and could not have been done without the aid of Sue Park, Field Engineer for National Instruments, and Walker Clark, Technical Sales Representative for National Instruments.

THIS PAGE INTENTIONALLY LEFT BLANK

I. INTRODUCTION

The free electron laser (FEL) has become a self-defense weapon that the U.S. Navy is interested in deploying aboard its ships. Although there are many challenges yet to overcome, the resulting product will provide the U.S. Navy with a weapon system that will allow it to recover space onboard ship, reduce the hazard of carrying hazardous ammunition stores and allow it to counter the increasing number of threats that are capable of supersonic flight and high-g maneuvers [Todd, 1997]. An inherent challenge to the shipboard operating environment, and the one investigated in this thesis, is sufficient alignment of the cavity mirrors of the laser in order to maintain proper operation. Misalignment of the mirrors causes the gain of the laser to be reduced, and can lead to the laser shutting off. This is a concern for the planned FEL weapons onboard ships, due to vibrations resulting from sea motion, ship machinery, and battlefield environment. These contributions can all contribute negatively to the operation of the FEL since it is critical that the electron beam and optical mode must substantially overlap for the laser to properly function. It has been shown through simulations at the Naval Postgraduate School that for a one megawatt (MW) FEL with cavity gain present, the maximum mirror tilt allowable is $180\mu\text{rad}$ [Crooker, 2002]. This tolerance level has been achieved in a laboratory environment at Duke University, which has been able to maintain stability to within $0.1\mu\text{rad}$ [Fiorani, 2002]. Although it may appear that there is no difficulty in maintaining mirror stability based on the achieved laboratory results and the predicted simulations, the shipboard environment is an unstable platform which has far greater dynamics to control than a stationary laboratory environment.

A. BASIC FEL PRINCIPLES

In its most basic form, FEL operation can be described as an electron source combined with an accelerator to impart added energy to the electrons, an undulator (also known as a wiggler) and a resonant optical cavity to capture the stimulated light emission and provide a means of optical gain as shown in Fig. 1.

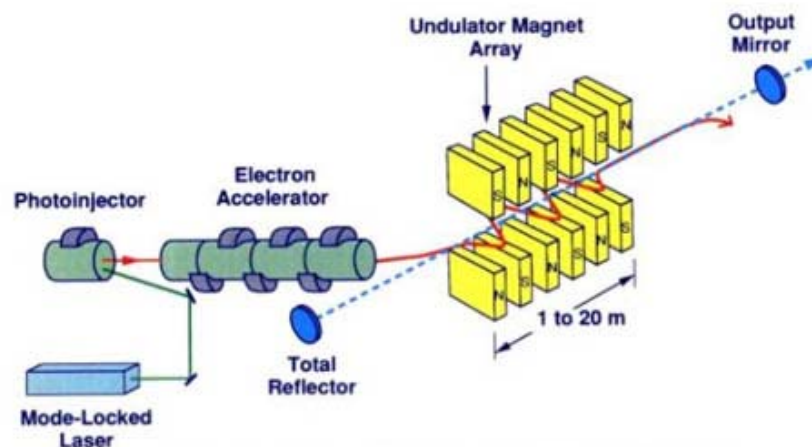


Figure 1. **Basic FEL Schematic** [from University of Maryland]

By carefully overlapping the laser light and the undulating electron beam, energy is transferred to the light beam from the oscillating electron beam. This process is enhanced by the optical cavity as the stored optical beam continuously interacts with new electrons traveling through the undulator as indicated by the "Optical Feedback" block of Fig. 2.

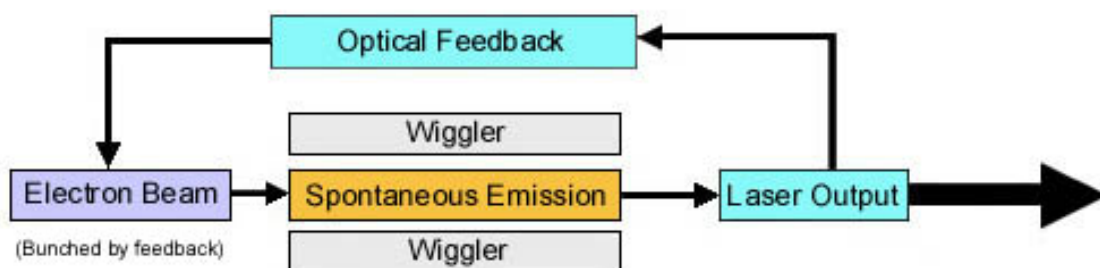


Figure 2. **Basic FEL Operation** [from University of Maryland]

The optical cavity of an FEL is designed to be a stable two-mirror type resonator (Fig. 3) in which a set of lowest-order gaussian beams can bounce back and forth between the optical cavities mirrors.

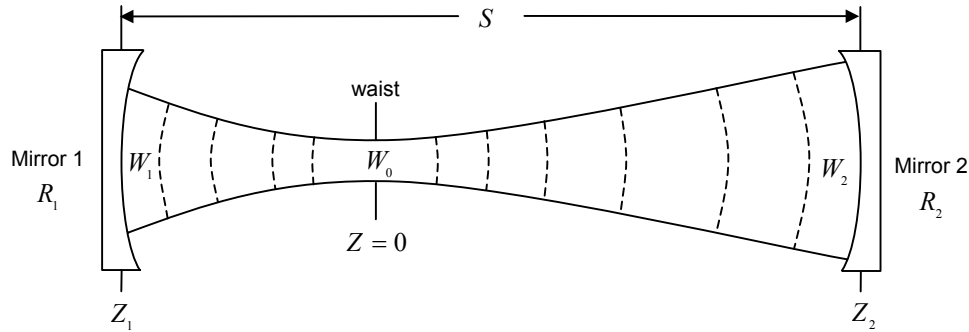


Figure 3. **Model of a Stable Two-Mirror Resonator** [from Fiorani]

This resonance traps the gaussian beam and forms an optical standing wave that is a fundamental requirement for lasing to occur. For lasing to actually occur in an FEL, the optical mode and the undulating electron beam must overlap. When vibrations occur, two situations may arise. Either the cavity mirrors can move with respect to each other and cause the lasing to stop since the optical cavity is no longer aligned or the undulator can move with respect to the fixed optical cavity and the electron beam will no longer overlap with the optical mode and the FEL will again stop lasing. Fig. 4 shows a highly exaggerated optical mode translation demonstrating the extreme effects vibrations can have on an FEL when attempting to maintain the alignment of the optical mode and undulator.

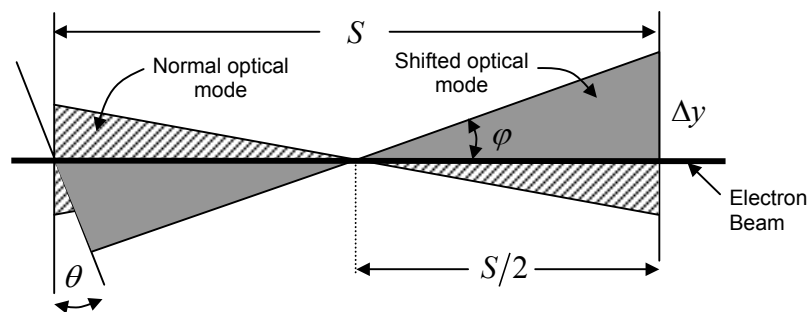


Figure 4. **Optical Mode Translation** (angles exaggerated) [from Fiorani]

B. SHIPBOARD INTEGRATION ISSUES AND SPECIFICATIONS

When operating in a shipboard environment, many considerations must be taken into account to maintain the stability of onboard equipment. In order to accomplish this, many options are available to the designer such as rigidity of the enclosure, incorporating mounting isolation supports and/or implementing active vibration control. Although the goal of this thesis is to investigate the use of active vibration control, when a combination of these methods are utilized in parallel, an extremely stable environment can be assured. One method of mounting isolation currently under contract for FEL's is being worked on by Energen, Inc of Lowell, Massachusetts (www.energeninc.com). This company completed simulations of a single dimension active vibration control support as part of a continuing contract to develop a physical three dimensional (3-D) active vibration isolation platform for FEL systems based on their one dimensional simulations [Kelly, 2003].

In order to determine the level of effectiveness when reducing vibrations, test procedures and specifications outlined in the Department of Defense instruction MIL-STD-167-1, Test Method Standards, and Office of the Chief of Naval Operations (OPNAV) instruction 9072.2, Shock Hardening of Surface Ships are utilized. The MIL-STD-167-1 Test Method Standard ",applies to all equipment intended for shipboard use or which must be capable of withstanding the environmental vibration conditions which may be encountered aboard naval ships." Under this instruction, equipment is tested at vibration frequencies from zero to approximately 33Hz while some newer surface ships include up to 50 Hz. In conjunction with this instruction, OPNAVINST 9072.2, Shock Hardening of Surface Ships, requires shock hardening for "all surface ships capable of operating in a combat shock environment." These instructional requirements along with known tolerances of the FEL serve as the basis and need for vibration control.

C. THESIS OBJECTIVES

The objectives of this thesis are to investigate active control methods for use in stabilizing the vibrations of laser cavity mirrors, and to demonstrate the effectiveness and limitations of the active controls. The investigations are analytical, numerical, and experimental, with the goal of leading to an understanding of the physics of the controlled systems. This understanding will be very useful in the ultimate implementation of controls for proposed FEL weapons systems on ships.

An analytical treatment of a theoretical model system is presented in Ch. II, and numerical simulations of the system driven by noise are investigated in Ch. III. The implementation and testing of a computer data acquisition system (LabVIEW) are discussed in Ch. IV, and laboratory experiments with a flexing metal strip are described in Ch. V. Conclusions and future work are stated in Ch. VI.

THIS PAGE INTENTIONALLY LEFT BLANK

II. THEORY

In this chapter, we consider the theory of the feedback control of the motion of a single-degree of freedom model system subject to random vibrations. The model system is discussed in Sec. A, the control and stability in Sec. B, and the combination of the gains in Sec. C. The development here is similar to the previous one by Fiorani (2002), although a number of improvements have been made.

A. MODEL SYSTEM

We consider a system with a single degree of freedom shown in Fig. 5. Other mechanical resonances may be present in an actual system, but it may be possible to identify these and add stiffness such that their resonance frequencies are pushed to sufficiently large values that the response is negligible. In Fig. 5, it should be noted that the actuator represents an ideal element that exerts an instantaneous force proportional to the instantaneous input voltage. The actual inertia, stiffness, or damping are considered to be lumped into the mass m , spring constant k , and damping coefficient c .

The equation of motion for the displacement $x(t)$ of the mass m from equilibrium is

$$m\ddot{x} = -kx - c\dot{x} + F(t) - G(x) , \quad (1)$$

where the dots denote time differentiation, and where $F(t)$ is the random external force and $G(x)$ is the control (actuator) force. We express Eq. (1) in the standard form

$$\ddot{x} + 2\gamma\dot{x} + \omega_0^2 x = f(t) - g(x) , \quad (2)$$

where the damping parameter is $\gamma = c/2m$, the natural angular frequency is $\omega_0 = (k/m)^{1/2}$, and the forces per unit mass are $f(t)$ and $-g(x)$. As we will show, an appropriate form of actuator force per unit mass in our case is

$$g(x) = \alpha\omega_0^2 x + 2\beta\omega_0\dot{x} , \quad (3)$$

where we have inserted appropriate factors of ω_0 so that the gains α and β are dimensionless. The factor of 2 in the second term is for later convenience.

For $\alpha, \beta > 0$, the result of Eq. (3) substituted into Eq. (2) is to apply forces opposite to both the displacement and the velocity. The most common controller is by far the PID type, where “P” stands for proportional, “I” for integral, and “D” for derivative. The case (3) thus corresponds to a PD controller.

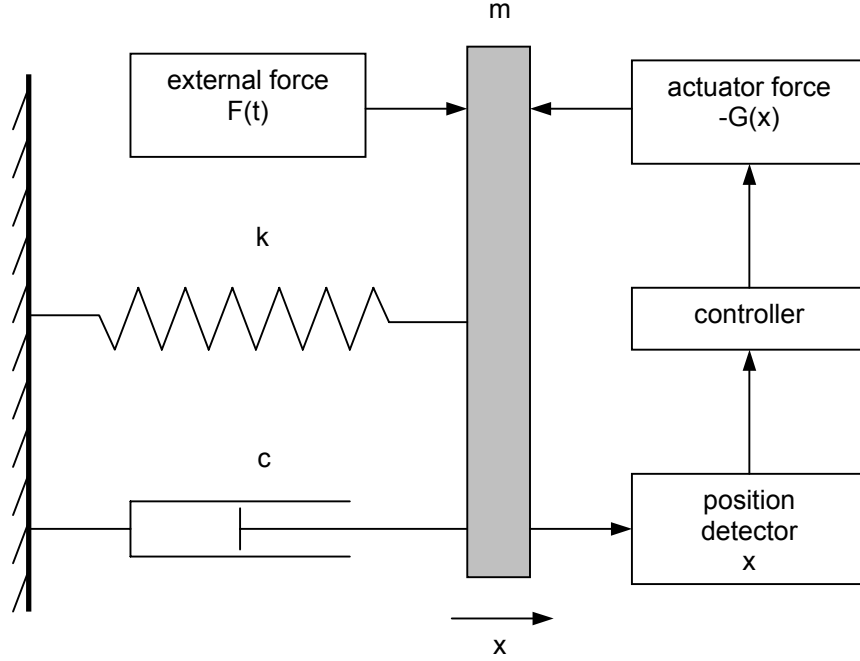


Figure 5. **Model system with one translational degree of freedom.** The objective is to determine the force $-G(x)$ such that the vibrations of m due to the force $F(t)$ are minimized.

B. CONTROL AND STABILITY

The effect of the control in our system can be readily investigated analytically. Substituting Eq. (2) into (1), and combining the displacement and velocity terms, yields

$$\ddot{x} + 2\Gamma\dot{x} + \Omega^2x = f(t) , \quad (4)$$

where the square of the effective natural angular frequency is

$$\Omega^2 = (1 + \alpha)\omega_0^2 , \quad (5)$$

and the effective damping parameter is

$$\Gamma = \gamma + \beta\omega_0 . \quad (6)$$

From Eq. (5), we observe that the effect of the proportional control α is to increase the natural frequency and thus stiffen the oscillator. From Eq. (6), the effect of the derivative control β is to increase the damping.

Positive feedback in our system corresponds to negative values of the gains α and β , which serve to lower the stiffness and damping, respectively. However, positive feedback does not necessarily lead to instability. The only stability criteria for our system is that the effective natural frequency (5) and effective damping parameter (6) are positive, which imply

$$\alpha > -1 , \quad (7)$$

and

$$\beta > -\gamma/\omega_0 . \quad (8)$$

For a monofrequency force per unit mass $f(t) = f_0\cos(\omega t)$, the steady state displacement is well-known (Fiorani, 2002) to be $x(t) = A \cos(\omega t - \varphi)$, where the amplitude is

$$A = \frac{f_o}{\sqrt{(\Omega^2 - \omega^2)^2 + 4\Gamma^2\omega^2}}, \quad (9)$$

and the phase is $\varphi = \tan^{-1}[2\Gamma\omega/(\Omega^2 - \omega^2)]$. In our model system, there is no limit to the upper values of the gains α and β in Eqs. (5) and (6). Hence, the effective natural frequency Ω and effective damping parameter Γ can be made arbitrarily large. From the Eq. (9), we thus find the response amplitude can be made arbitrarily small. This will be explicitly shown in the next section.

C. GANGING OF THE GAINS

The most effective means of damping shocks (abrupt or transient vibrations) is to have a *critically damped* system (Fiorani, 2002), which occurs when the damping parameter equals the natural frequency. We thus choose this to be the case for our system. According to Eq. (4), critical damping corresponds to $\Gamma = \Omega$. From Eq. (5) and (6), the condition $\Gamma = \Omega$ yields

$$\beta = \sqrt{1 + \alpha} - \frac{\gamma}{\omega_o}. \quad (10)$$

We initially did not recognize this “ganging” of the gains (that is, a unique relationship between the two gains). We simply set $\beta = \omega_o$, which corresponds to critical damping only for $\alpha = 0$. The error became apparent when we performed numerical simulations (Chapter III).

We suppose that the noise force per unit mass $f(t)$ is “white”; that is, the amplitude as a function of frequency is constant. The average steady state displacement will then have the displacement amplitude equal to Eq. (9). Fig. 6

shows graphs of the displacement amplitude A as a function of frequency according to Eq. (9) for $f_o = \omega_o = 1$ and $\gamma = 0.1$. Curve (a) corresponds to zero gains ($\alpha = \beta = 0$). Curves (b), (c), and (d) correspond to proportional gains of $\alpha = 0, 10^2$, and 10^4 , respectively, where the derivative gain β is ganged to α according to Eq. (10), so that the damping is critical in each case.

The natural frequencies of curves (b), (c), and (d) in Fig. 6 are approximately $\Omega = 1, 10$, and 100 , respectively, but do not correspond to resonance peaks due to the critical damping. A prominent feature of the curves is the universal asymptotic roll-off at higher frequencies. This corresponds to the *inertia-controlled regime*, where the motion becomes approximately independent of the natural frequency and the damping. From Eq. (9), the amplitude in this regime is given by

$$A(\omega \gg \Omega) = \frac{f_o}{\omega^2} . \quad (11)$$

which rolls off as $A \propto \omega^{-2}$. This corresponds to slope -2 on a log-log scale, which is confirmed in Fig. 6.

For critical or overdamped motion, the maximum displacement occurs in the limit of zero frequency (*stiffness-controlled regime*), and is given by f_o/Ω^2 , or

$$A_{\max} = \frac{f_o}{(1 + \alpha)\omega_o^2} . \quad (12)$$

The maximum displacement can be made as small as desired by choosing the proportional gain α to be sufficiently large according to Eq. (12).

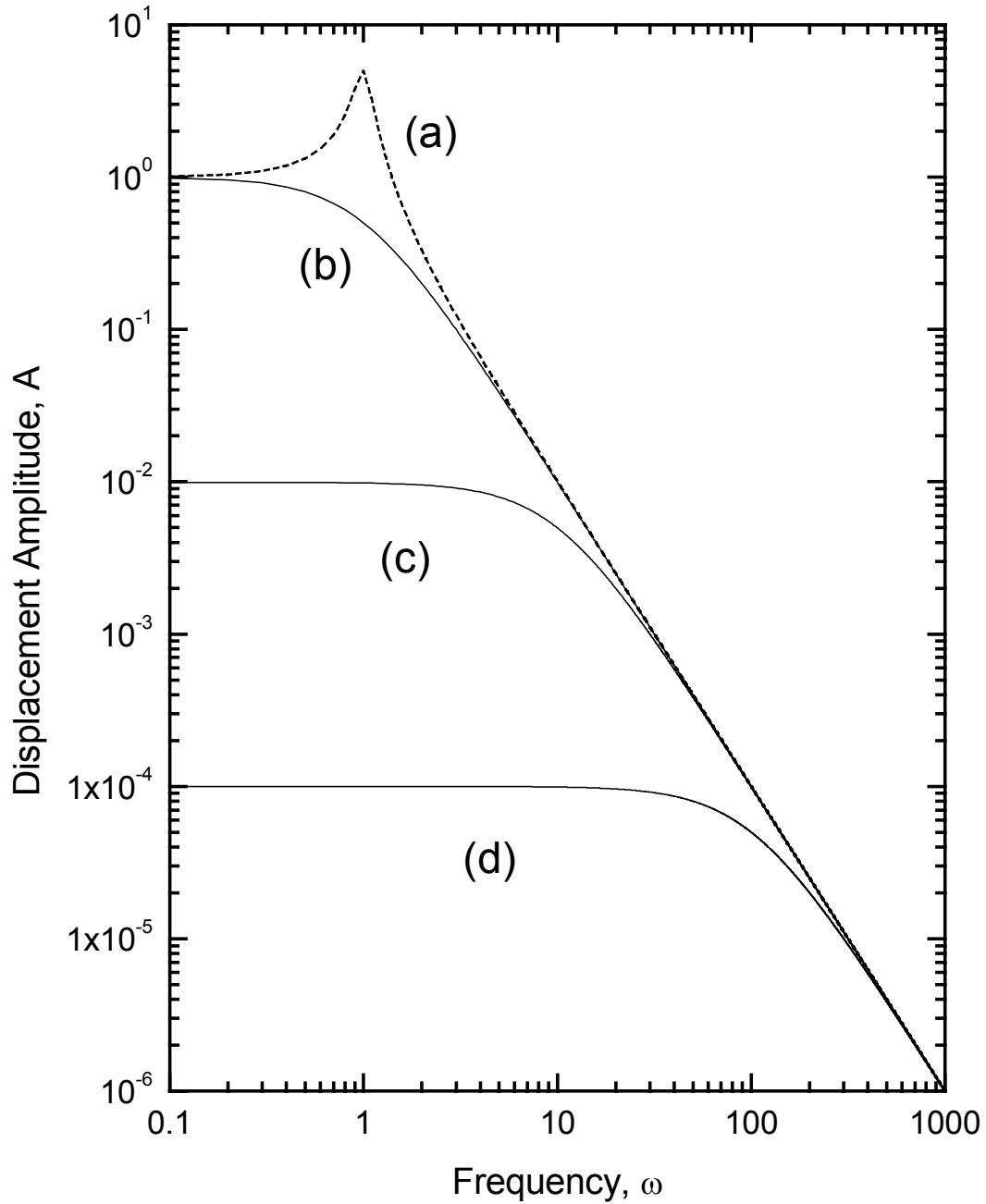


Figure 6. **Displacement amplitude for an oscillator driven by white noise, for different values of the feedback control proportional gain α and derivative gain β .** Curve (a) corresponds to zero gains ($\alpha = \beta = 0$). Curves (b), (c), and (d) correspond to $\alpha = 0$, 10^2 , and 10^4 , respectively, where in each case β is chosen so that the damping is critical.

THIS PAGE INTENTIONALLY LEFT BLANK

III. NUMERICAL SIMULATIONS

In this chapter, we present numerical simulations of a damped noise-driven oscillator whose response is reduced due to proportional and derivative feedback control. There are several reasons why it is important to perform numerical simulations. First, although the theory in Chapter II appears to be beyond question, the simulations give independent confirmation. Second, the simple simulations of the one-degree-of-freedom system here are a first step in dealing with more realistic and complicated several-degree-of-freedom systems in a future thesis. Third, although it appears that the analytical theory for the inclusion of integral control of a single-degree-of-freedom system can be done, a physical interpretation on the level of the proportional and derivative control is not clear. Hence, it is important to be able to conduct numerical simulations to confirm the theory and to develop intuition about this third type of control.

A. DAMPED NOISE-DRIVEN OSCILLATOR

We begin with a damped harmonic oscillator driven by noise, which is described by Eqs. (2) and (3):

$$\ddot{x} + 2\gamma\dot{x} + \omega_0^2 x = f(t) - g(x, \dot{x}) , \quad (13)$$

where

$$g(x, \dot{x}) = \alpha\omega_0^2 x + 2\beta\omega_0\dot{x} , \quad (14)$$

where $f(t)$ is a broadband noise force per unit mass, and $-g(x, dx/dt)$ is the control force, which equals zero in this section.

The first problem is to obtain a numerical noise source $f(t)$. We originally thought that $f(t)$ must be continuous, as it is in actual physical cases. However, a random number generator (which is available in any compiler) can serve as the source, as we now show. We subtract 0.5 from each random number between 0.0 and 1.0, so that the average value is zero, and then multiply by an arbitrary factor of 100 so that the frequency spectrum has a convenient scale. The resultant fast Fourier transform (FFT) of a time series with a dimensionless time step $\Delta t = 0.01$ and total number of time points equal to $2^{14} = 16,384$ is shown in Fig. 7(a). The software OriginTM was used for this and all subsequent FFT's. Averaging the frequency spectrum over 20 adjacent points yields the frequency spectrum shown in Fig. 7(b). The noise is white (uniform spectrum) and has a dimensionless cutoff frequency $f_c = 50$. The cutoff frequency occurs because the highest frequency corresponds to a period of $2\Delta t$ (Nyquist limit). The frequency is thus $f_c = 1/(2\Delta t) = 1/(2 \cdot 0.01) = 50$, which is indeed the case as observed in Fig. 7.

We choose the dimensionless natural frequency of the oscillator to be $f_o = 1.0$. The dimensionless natural angular frequency is then $\omega_o = 2\pi$. We choose the damping parameter to be $\gamma = 0.1 \omega_o$ which corresponds to a quality factor of $Q = 5.0$. To numerically simulate the motion according to Eq. (13) with the noise force, we employ the standard Euler-Cromer method with dimensionless time step $\Delta t = 0.01$. The computer program is listed in Appendix A. The FFT for $2^{14} = 16384$ time points of $x(t)$ is shown in Fig. 8(a). Averaging this frequency spectrum over 20 adjacent points yields the smoothed spectrum in Fig. 8(b). Henceforth in this chapter, every displayed spectrum will be smoothed in the same way.

Fig. 8(b) has all of the correct features of a frequency response curve. For example, the peak occurs at the correct resonance frequency $f_o = 1.0$. Also, the width corresponds to the correct quality factor $Q = 5.0$, and the maximum

response is correctly given by Q-amplification (the maximum amplitude is approximately Q times the amplitude at zero frequency).

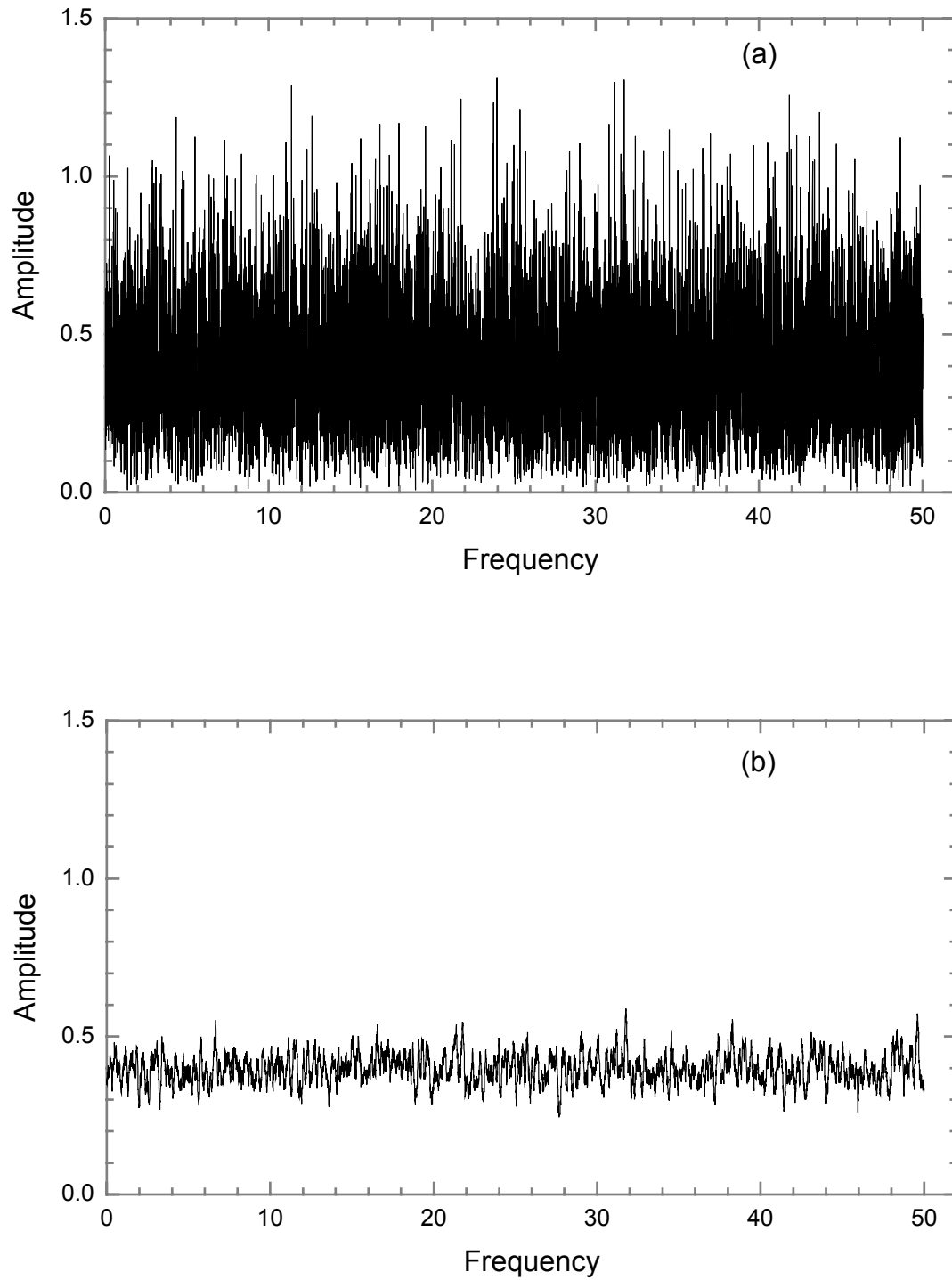


Figure 7. **(a) Fast Fourier transform (FFT) of numerical random noise with time step 0.01. (b) Data from (a) smoothed over 20 adjacent points.** The noise is white. The dimensionless cutoff frequency of 50 corresponds to the Nyquist limit of the noise.

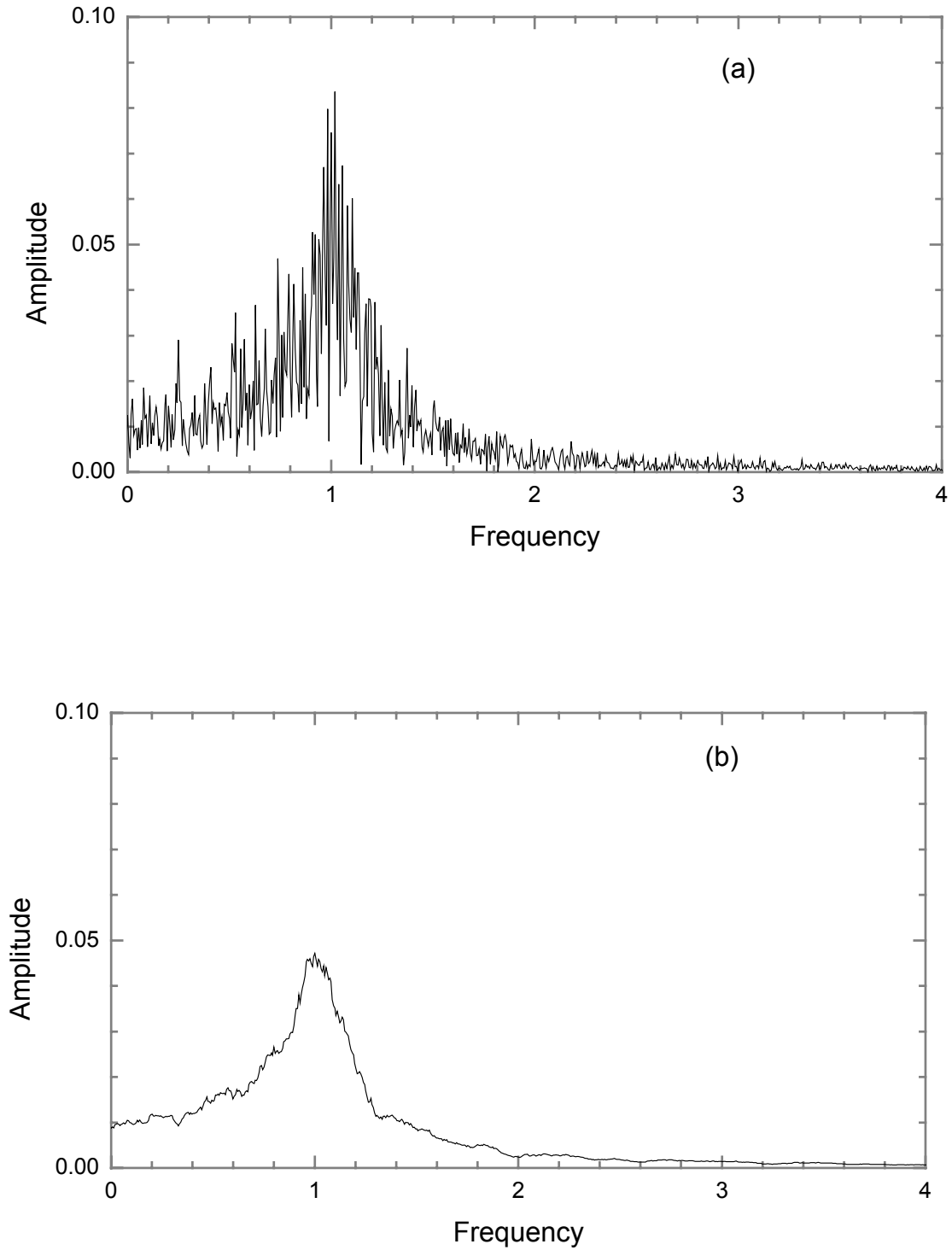


Figure 8. **(a) FFT of the position $x(t)$ of an oscillator driven by random noise. (b) Data from (a) smoothed over 20 adjacent points.** The dimensionless natural frequency of the oscillator is $f_0 = 1.0$, and the damping parameter is $\gamma = 0.1 \omega_0$ (quality factor $Q = 5.0$).

B. PROPORTIONAL (STIFFNESS) CONTROL

In this section, we investigate numerical simulations with proportional control, or the dimensionless gain $\alpha > 0$ in Eq. (14). The derivative control gain β remains equal to zero. As evident in Eq. (14), and described in Chapter II, the proportional control has the effect of stiffening the oscillator or increasing the natural frequency. We use the same oscillator parameters as in the previous section, as well as the same simulation parameters. For the purpose of comparison, the frequency spectrum for zero proportional control gain ($\alpha = 0$) is shown in Fig. 9(a), which is the same as Fig. 8(b) except for the scales.

The gain $\alpha = 3.0$ yields the frequency spectrum in Fig. 9(b). The resonance frequency is now doubled from $f_0 = 1.0$ to 2.0. From Eqs. (7) and (8), this doubling occurs because the effective natural angular frequency is $[\omega_0^2 + \alpha\omega_0^2]^{1/2} = (1 + \alpha)^{1/2}\omega_0$, which has the value $2\omega_0$ for $\alpha = 3.0$. Note that the response decreases at the resonance peak. This behavior occurs because the displacement amplitude at resonance is approximately inversely proportional to the natural frequency for constant values of the force amplitude, damping parameter, and mass [refer to Eq. 9]. Note that the displacement amplitude at zero frequency also decreases. This occurs because the amplitude is inversely proportional to the stiffness (quasistatic stiffness-controlled limit in which Hooke's law applies). The stiffness has quadrupled because the natural frequency is doubled, which explains the decrease in amplitude by a factor of 4. Finally, note that the width of the resonance remains the same, which occurs because the damping parameter is the same. The quality factor thus doubles, which is consistent with the observed Q-amplification by an approximate factor of 10.

The frequency spectra for proportional gains of $\alpha = 15.0$ and 63.0 are shown in Figs. 9(c) and 9(d), respectively. These gain values were chosen because the first corresponds to an effective natural frequency of 4.0 and the second an effective natural frequency of 8.0. The numerical time step Δt in the second case had to be halved to $\Delta t = 0.005$ due to the greater frequency of the

motion at the peak. It is interesting that the need for this arose from the observation that the resonance peak occurred at a frequency of 8.1 for $\Delta t = 0.01$, rather than the correct frequency of 8.0. The results for the two gain values are in accord with the features stated above for the gain of $\alpha = 3.0$.

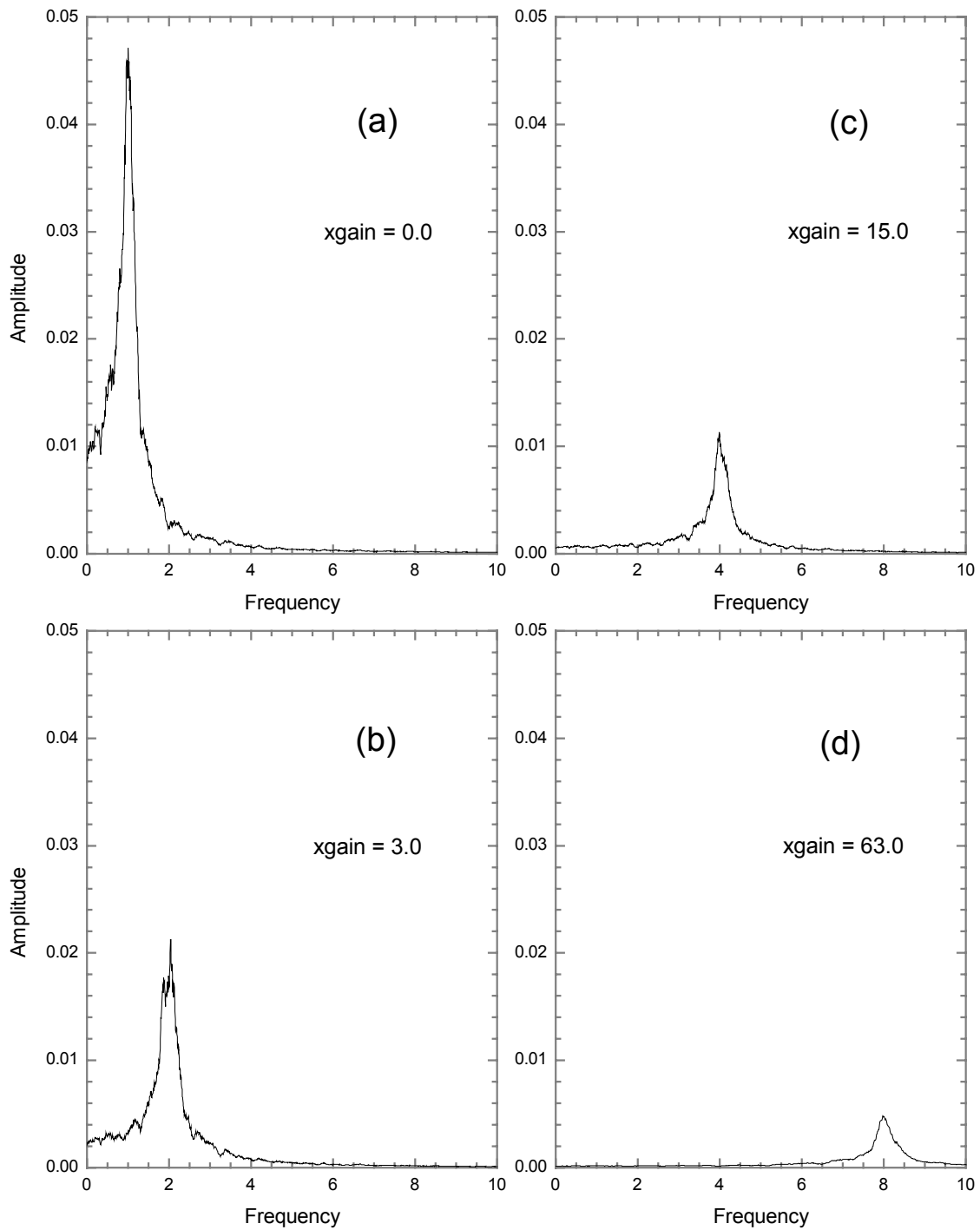


Figure 9. **FFT's for different values of the proportional control gain α (or “xgain” in the computer program and in the above graphs).** The effect is to monotonically increase the natural frequency of the oscillator from the value 1.0 in (a) to the value 8.0 in (d).

C. DERIVATIVE (RESISTIVE) CONTROL

In this section, we investigate numerical simulations with derivative control, or the dimensionless gain $\beta > 0$ in Eq. (14). The proportional control gain α , which was investigated in the previous section, is equal to zero. As evident in Eqs. (13), and described in Chapter II, the derivative control has the effect of damping the oscillator. We use the same oscillator parameters as in the previous sections, as well as the same simulation parameters. As in the previous section, for the purpose of comparison, the frequency spectrum for zero derivative control gain ($\beta = 0$) is shown in Fig. 10(a).

The gain $\beta = 0.1$ yields the frequency spectrum in Fig. 10(b). From Eqs. (13) and (14), the effective damping parameter is doubled from $\gamma = 0.1$ to 0.2. The motion is still underdamped, as evidenced by the resonance peak, but the peak amplitude is reduced by approximately a factor of 2. Also, the peak is clearly asymmetric, which occurs due to the substantial damping. Fig. 10(c) shows the frequency spectrum for $\beta = 0.9$, which corresponds to the effective damping parameter of 1.0 or $\gamma = \omega_0$. The oscillations are now critically damped (Chapter II). The resonance peak no longer exists. Fig. 10(d) shows the frequency spectrum for $\beta = 1.9$, which corresponds to an effective damping parameter of twice the critical value. The motion is now overdamped. It is interesting that the frequency spectrum is not substantially lowered compared to the critical case. Also, note that the zero-frequency amplitudes are the same in all four cases, which occurs because the damping is irrelevant in this quasistatic stiffness-controlled limit.

As stated in Chapter II, overdamping is not desirable because of the slow approach to equilibrium after strong transient vibrations (“shocks”). We thus employ a derivative control gain that yields effective critical damping.

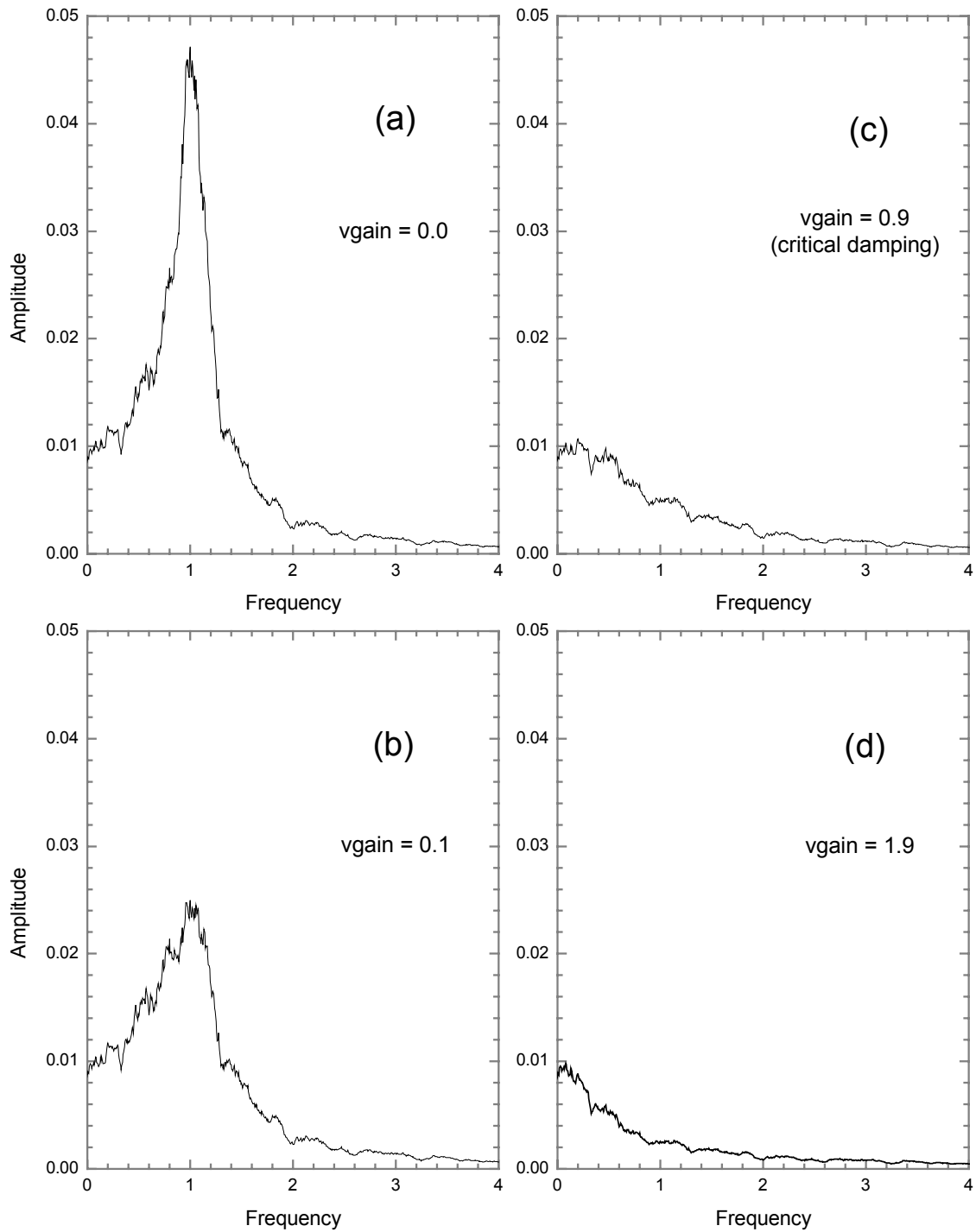


Figure 10. **FFT's for different values of the derivative control gain β (or "vgain" in the computer program and in the graphs above).** The effect is to monotonically increase the damping of the oscillator from the value $\gamma = 0.1$ in (a) to the value 8.0 in (d).

D. PROPORTIONAL-DERIVATIVE (PD) CONTROL

We now combine the proportional and derivative controls, which were investigated separately in Sections B and C. Fig. 11 shows the frequency spectra for a fixed derivative control gain of $\beta = 0.9$, which corresponds to effective critical damping of the original oscillator. For comparison, the frequency spectrum for zero proportional gain α is shown in Fig. 11(a), which is identical to Fig. 10(c) except for the scales. Shown in Figs. 11(b,c,d) are the frequency spectra for successive proportional control gains of $\alpha = 3.0, 15.0$, and 63.0 . As in Section B, these gain values correspond to effective natural frequencies of $2.0, 4.0$, and 8.0 , respectively. A problem is immediately apparent in the three spectra: resonant peaks occur. This behavior is due to the fact that the effective damping parameter does *not* correspond to critical damping once the proportional control gain is not zero. As the proportional gain is increased, the natural frequency increases, so the motion becomes more and more underdamped if the derivative control gain remains fixed.

The solution to the problem is clear: To maintain an effective critical damping parameter $\gamma = \omega_0$, we must corresponding increase the derivative control gain. Fig. 12 shows the results of this “ganging of the gains” for proportional gains of $\alpha = 3.0, 15.0$, and 63.0 . The corresponding values of the derivative control gain are $\beta = 1.9, 3.9$, and 7.9 . The resonance peaks no longer occur. In Fig. 12(d), the maximum response (at zero frequency) is reduced by approximately a factor of 50 of that for the critically damped oscillator with no proportional gain [Fig. 12(a)].

According to the theory, there is no upper limit of the values of the control gains. That is, positive feedback cannot occur for the model system. The response can thus theoretically be reduced arbitrarily close to zero. This motivated us to perform numerical simulations for large gain values, and to compare the results to the theory. Figs. 13(c) and 13(d) show frequency spectra on log-log scales for the gain values $\alpha = 10^2, \beta = 10$, and $\alpha = 10^4, \beta = 10^2$,

respectively. For comparison, the frequency spectra for zero gains and the effectively critically damped ($\alpha = 0.0$, $\beta = 0.9$) oscillator are shown in Figs. 13(a) and 13(b), respectively. Note that all graphs have the same scales.

The gain values $\alpha = 10^2$ and $\beta = 10$ correspond to an effective natural frequency of approximately 10 with approximate effective critical damping, while the gain values $\alpha = 10^4$ and $\beta = 10^2$ correspond to an effective natural frequency of approximately 100 with approximate effective critical damping. These higher frequencies necessitate a smaller numerical time step which, in turn, necessitates more time points. For all four graphs, the time step was reduced to $\Delta t = 0.001$ (from 0.01), and the number of time points was increased to $2^{16} = 65,536$ (from $2^{14} = 16,384$). The simulation data terminate at the cutoff frequency $f_c = 1/(2\Delta t) = 500$, which is the maximum frequency of the noise. Initial results of Figs. 13(a) and 13(b) disagreed with previous results in this section. We eventually found that the problem was that the software (Origin) surprisingly gives different spectral amplitudes of the noise depending upon the total number of time steps. Specifically, doubling the number of time steps from 2^N to 2^{N+1} causes the spectral amplitude of the noise to decrease by the factor $2^{1/2}$. We were unable to find any options in the software to maintain a constant amplitude, so we made the appropriate adjustment in our computer program (Appendix A).

The dotted curves in Fig. 13 correspond to the theory (Chapter II). All numerical simulations agree with the theory in the stiffness-controlled regions (frequency significantly less than the natural frequency). For $\alpha \gg 1$, the stiffness-controlled amplitude varies inversely as α , and the frequency spectrum rolls off in the vicinity of the natural frequency which is proportional to $\alpha^{1/2}$. At higher frequencies (inertia-controlled regions), the theoretical curves are identical, which is the universality discussed in Chapter II. The deviations of the simulations from the theory here are due to an insufficiently small time step. We established this by performing simulations with the time step reduced by a factor of 10 to $\Delta t = 0.0001$. The data are not shown here because the large number of

time points ($2^{19} = 524,288$), which yielded very large data files (10's of megabytes) when the frequency spectra were computed.

It is surprising that there is substantially greater numerical error in Fig. 13(a) than 13(b), where the only difference is that the latter case is critically damped. Apparently the numerical method is more accurate for increased damping. The greater error at higher frequencies in Fig. 13(d) compared to 13(c) is evidently due to the greater amplitude of the motion in this region, which is due to the proximity of the natural frequency. This greater amplitude yields greater error due to a lack of a sufficiently small time step.

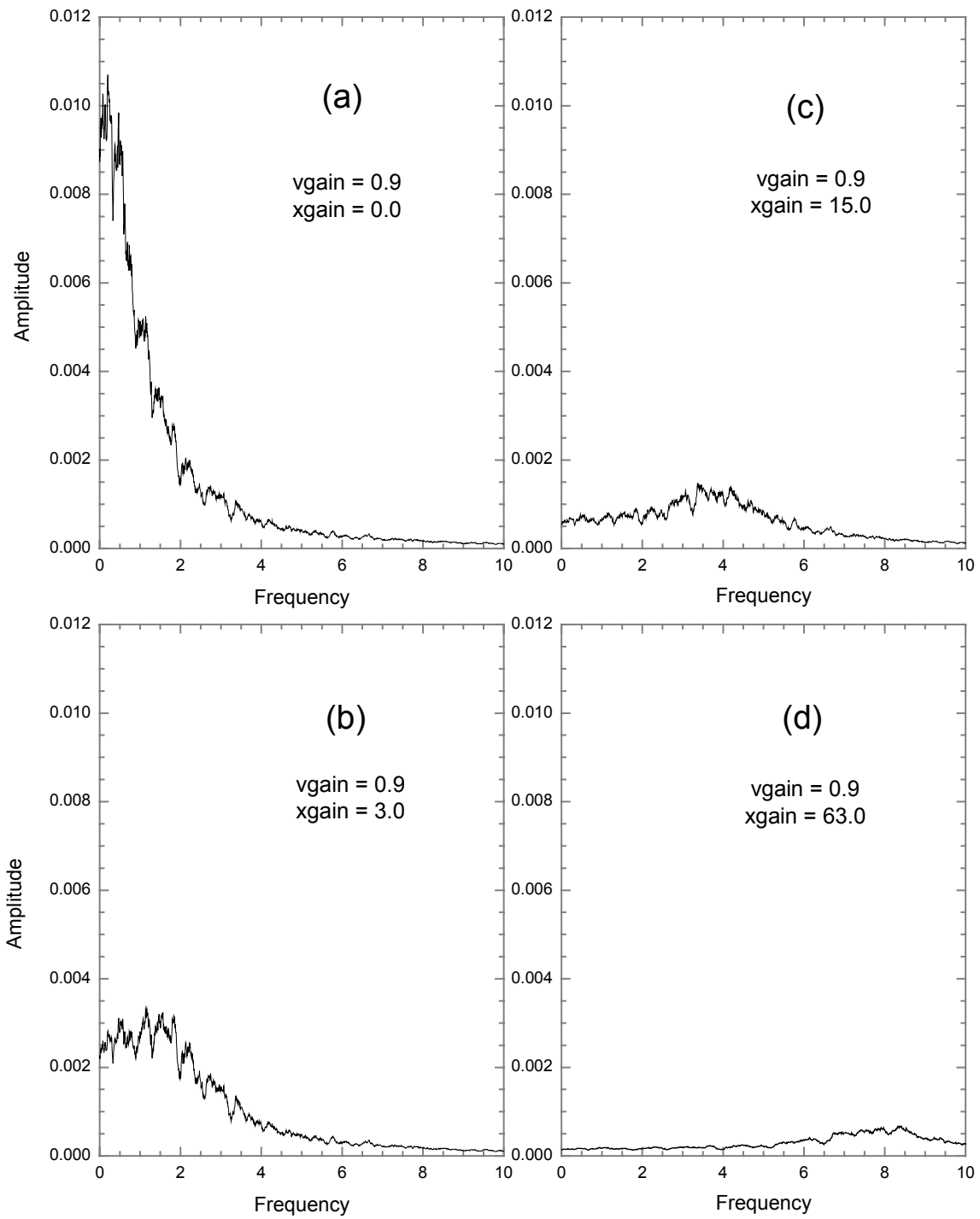


Figure 11. **FFT's for different values of the proportional control gain α (xgain) for fixed derivative control gain β (vgain).** The motion is critically damped in (a), but is underdamped in (b), (c), and (d) as evidenced by the resonance peaks.

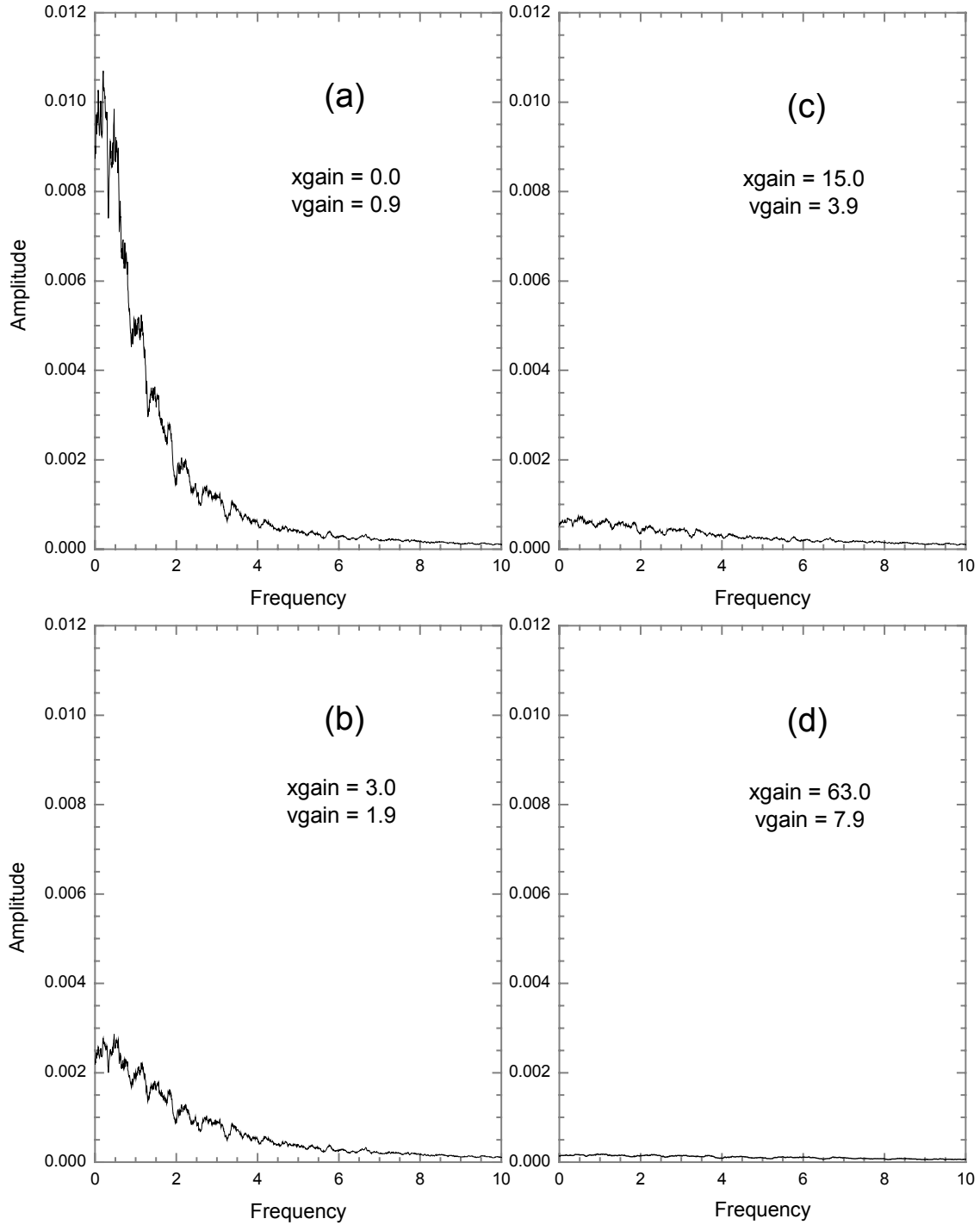


Figure 12. **FFT's for different values of the proportional control gain α (x_{gain}) and for corresponding values of the derivative control gain β (v_{gain}) such that the motion is effectively critically damped in each case. This removes the resonance peaks in Fig. 3.D.1.**

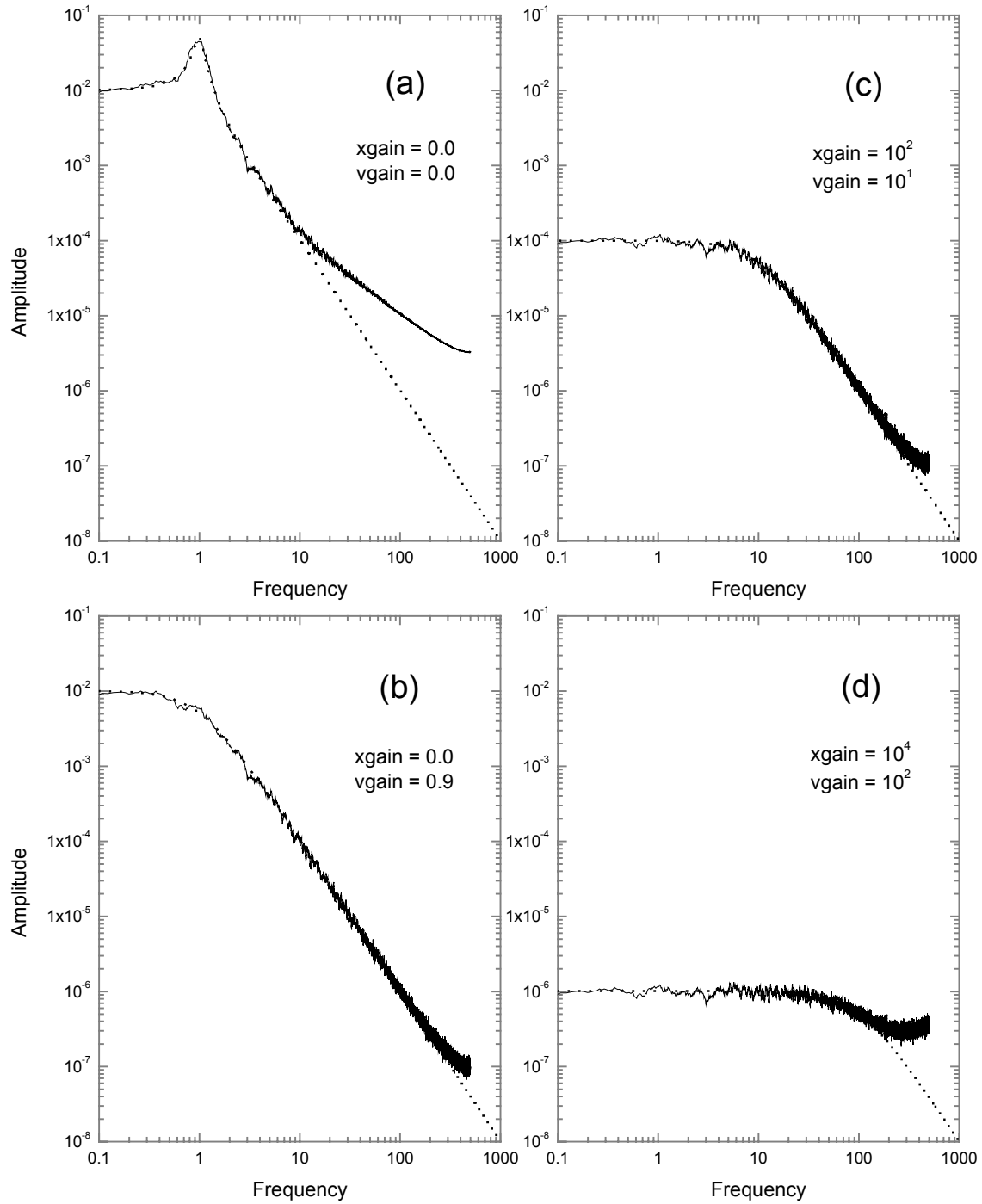


Figure 13. **FFT's for different values of the control gains, which are large in (c) and (d). The dotted curves correspond to the theory.**

IV. LABVIEW IMPLEMENTATION

Prior to implementing LabVIEW as the controller in our system, tests of the input and output sampling rates (Secs. A and B), resolution (Sec. C) and the loop rate (Sec. D) were performed to verify the data acquisition system was operating correctly. After confirming the operating characteristics of the data acquisition system, it was implemented as a controller in a simulation of our physical model system (Sec. E). This simulation consists of a series LC resonant circuit that is the electrical equivalent of the mechanical system shown previously in Fig. 5, the single-degree-of-freedom oscillator. In the experimental (Ch. V), we are concerned with reducing vibrations in the system which result from displacements of the flexing strip. In the electrical equivalent circuit, the voltage across the capacitor corresponds to the displacement of the vibrating strip. This voltage is fed to the controller, the LabVIEW data acquisition system, and then returned to the system as the control drive voltage $-G(x, dx/dt)$. The results from the electrical equivalent circuit are then verified against the numerical simulations of Chapter III to verify that the LabVIEW control system was operating correctly.

Initially the controller consisted of National Instruments LabVIEW 7 Express software, PCI 7030/6030E data acquisition board (DAQ) and a BNC-2090 terminal block. In tests conducted to verify the operation of the LabVIEW software and hardware, the DAQ was found to have a loop rate of approximately 1kHz. The loop rate is defined as acquiring a signal with the DAQ with an analog input, processing the signal and then outputting the signal through the DAQ'S analog output. Based on the Nyquist criterion, this theoretically limited our upper frequency limit to 500Hz. This limitation was not acceptable for our research so the DAQ was replaced with a PCI 7041/6040E DAQ that has a benchmark loop rate of 26kHz and a corresponding upper theoretical frequency limit of 13kHz. The tests outlined in Secs. A through D were carried out on each DAQ. Results of the tests below are for the NI PCI 7041/6040E DAQ only although the testing procedure was the same for the NI PCI 7030/6030E.

A. DAQ INPUT SAMPLING RATE

The input sampling rates were verified using the DAQ in conjunction with an HP33120A function generator and an Agilent Infiniium Oscilloscope. The signal from the function generator was sent to both the DAQ and the oscilloscope for comparison purposes. For the data acquisition system, the LabVIEW VI, "1 Channel Simple Scope.vi" shown in Figs. 14 and 15 was used to display the input signal and for visual comparison to the oscilloscope trace. (The traces for both the data acquisition system and the oscilloscope matched well until the function generator was raised to frequencies above 10kHz.)

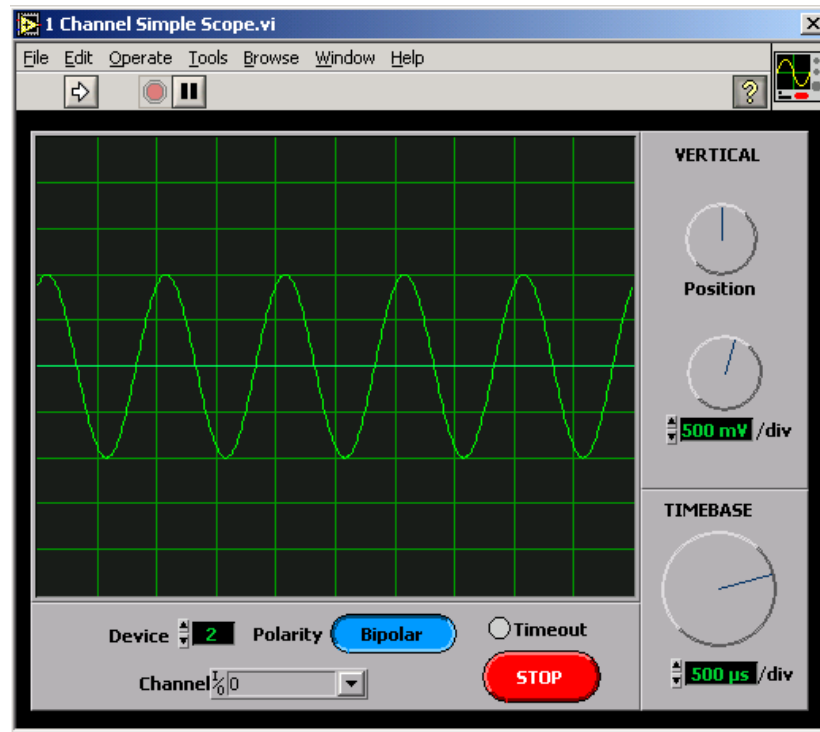


Figure 14. **'1 Channel Simple Scope.vi' Front Panel.** The user interface for '1 Channel Simple Scope.vi'.

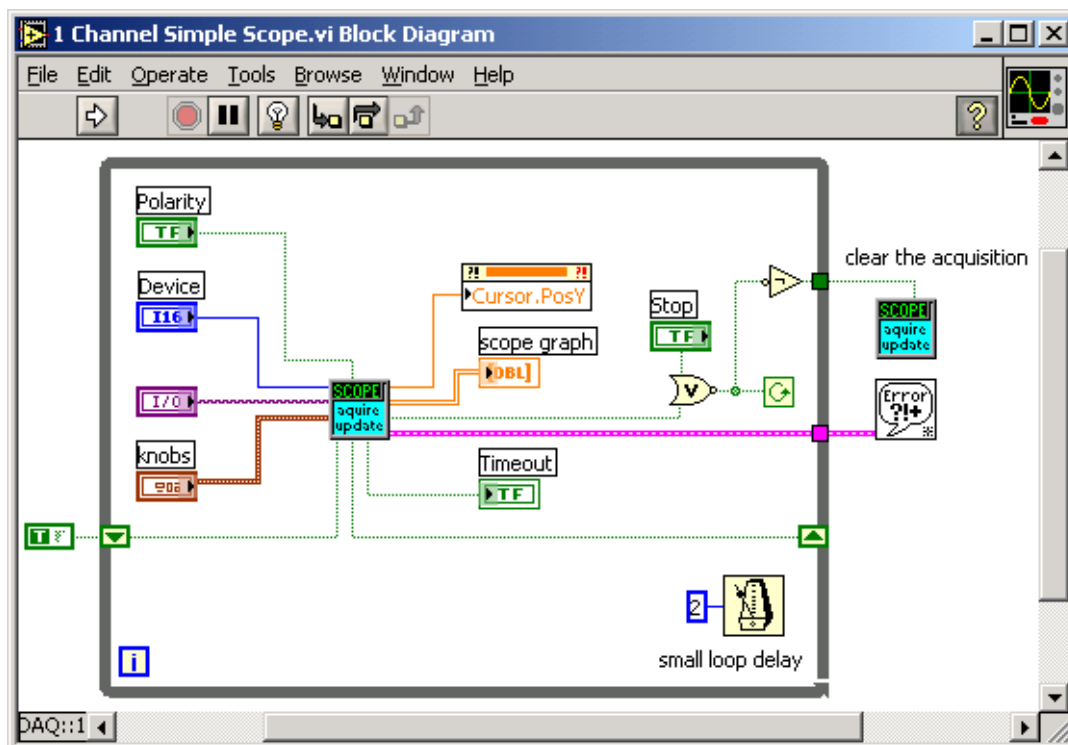


Figure 15. **'1 Channel Simple Scope.vi' Block Diagram.** The functional diagram of '1 Channel Simple Scope.vi'.

B. DAQ OUTPUT SAMPLING RATE

The output sampling rates were verified using the DAQ in conjunction with both an HP33120A function generator and an Agilent Infiniium Oscilloscope. The output signal was generated within LabVIEW with the sample VI "Benchtop Function Generator.vi" (Figs. 16 and 17) and output to the oscilloscope. In order to verify the output signal the function generator was set to the same frequency and amplitude as the LabVIEW VI and output to the second channel of the oscilloscope for direct comparison. The output sampling rate was verified and the DAQ is capable of outputting smooth waveforms to above 10kHz.

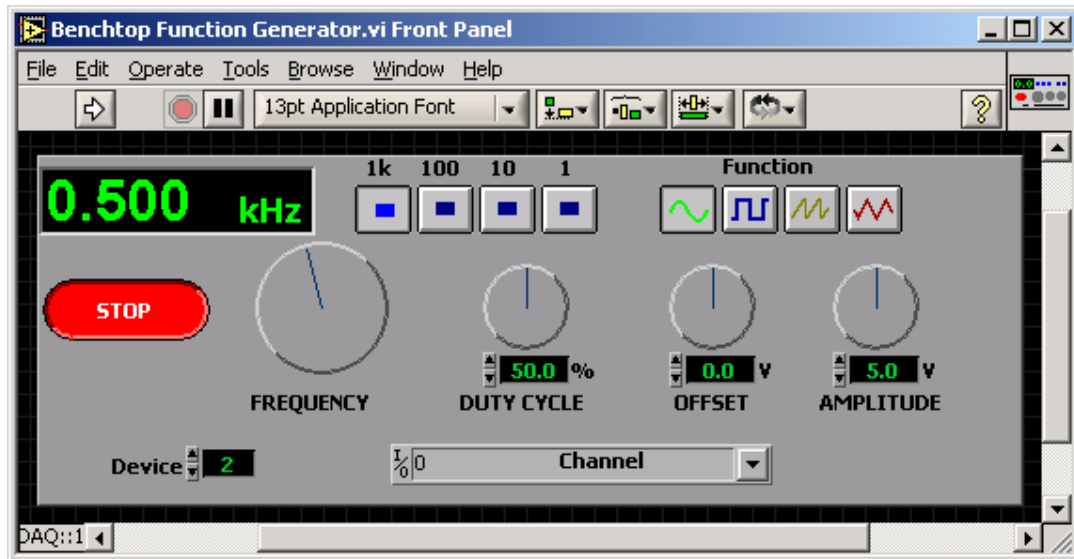


Figure 16. 'Benchtop Function Generator.vi' Front Panel. The user interface for 'Benchtop Function Generator.vi'.

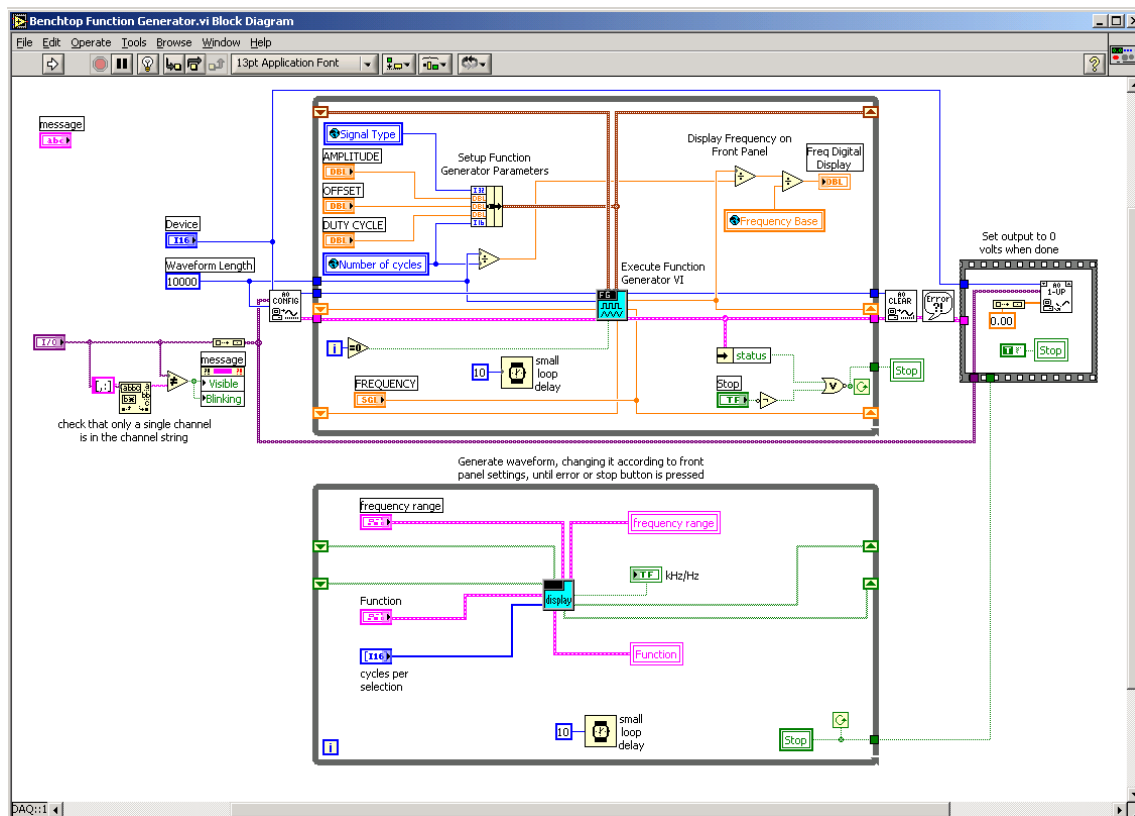


Figure 17. 'Benchtop Function Generator.vi' Block Diagram. The functional diagram of 'Benchtop Function Generator.vi'.

C. DAQ RESOLUTION

The DAQ resolution limits were determined utilizing a simple voltage divider circuit, illustrated in Fig. 18.

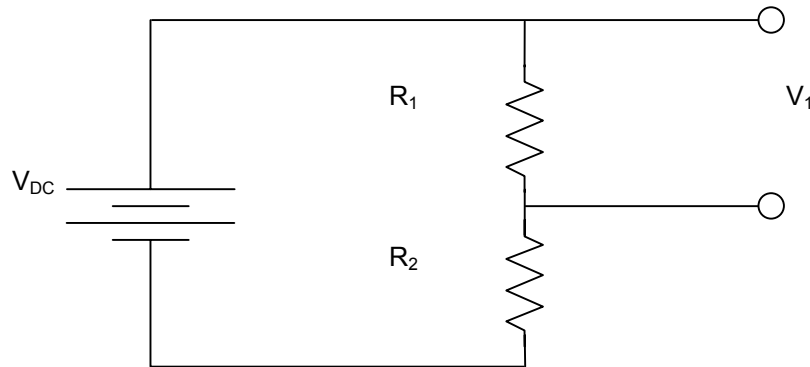


Figure 18. **Voltage divider circuit for DAQ resolution testing.** This simple voltage divider was used to fix the value of V_1 to a value on the order of one resolution step to determine the resolution of the DAQ.

The voltage across the resistor R_1 was fed into the DAQ analog input and displayed using the sample VI "Single Point Voltage Measurement.vi" shown in Figs. 19 and 20. The NI PCI 7041/6040E is capable of 12bit resolution measurements. In order to set the voltage across R_1 to the 12bit resolution step, the resistance R_1 and R_2 were chosen so that when V_{DC} was set to 1V it would yield the first step and then when V_{DC} was changed to 2V it would be at the next resolution step. The results confirmed the 12bit resolution accuracy of the DAQ.

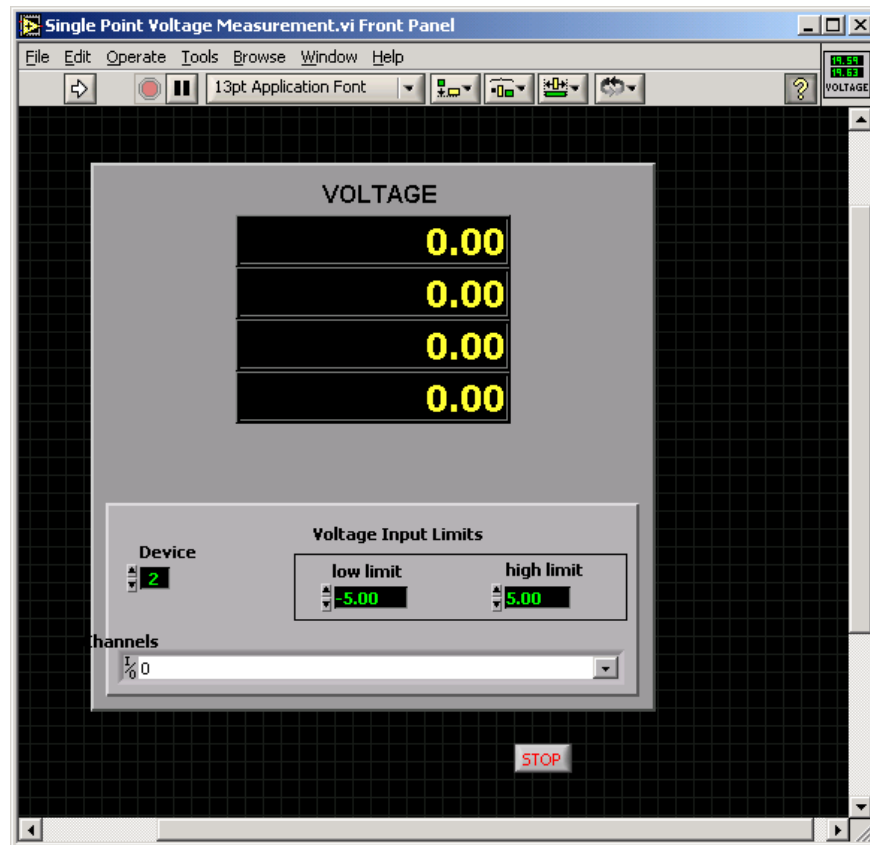


Figure 19. **'Single Point Voltage Measurement.vi' Front Panel.** The user interface for 'Single Point Voltage Measurement.vi'.

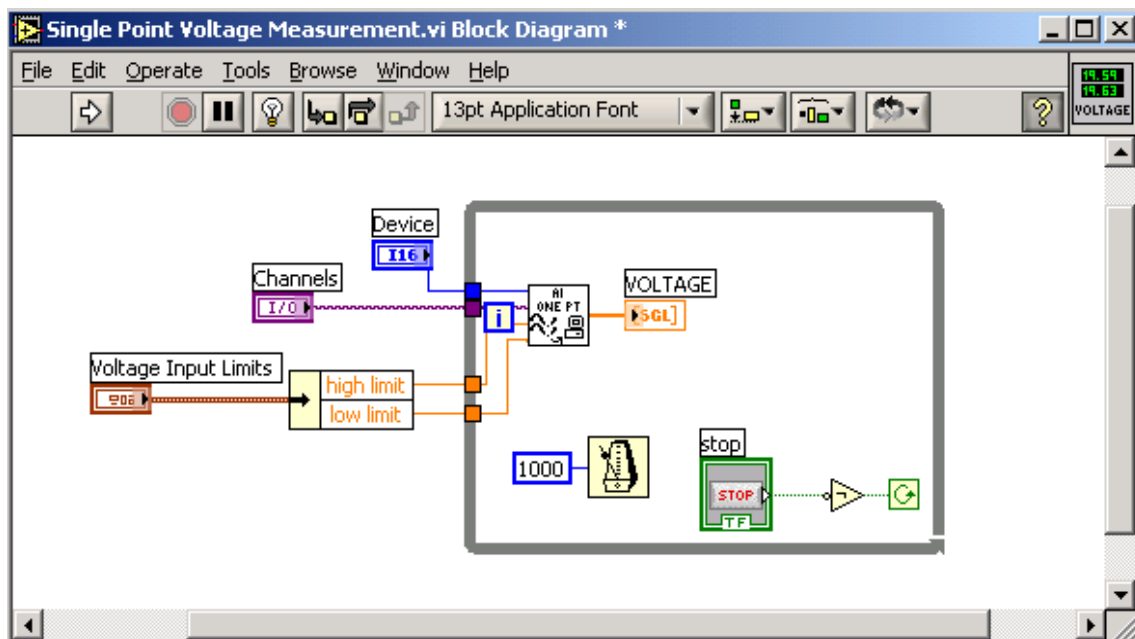


Figure 20. **'Single Point Voltage Measurement.vi' Block Diagram.** The functional diagram of 'Single Point Voltage Measurement.vi'.

D. DAQ LOOP RATE

The loop rate for the DAQ is not simply the lesser of the input sampling rate or the output sampling rate but a small fraction of the two. This reality results from the DAQ processor performing many tasks in a single loop not limited to the following: analog to digital conversion of the input signal, memory allocation, basic processing computations and a digital to analog conversion of the output signal. For the NI PCI 7030/6030E, the input and output sampling rates are both 100,000 samples per second (100kHz) but the NI benchmark loop rate is 1kHz. This value was achieved using the "Real Time PID Control.vi" sample shown in Figs. 21 and 22 with the PID functionality removed so the input was fed directly to the output. The DAQ was then replaced as discussed previously with the NI PCI 7041/6040E to enable loop rates on the order of 26kHz. Once again using the modified version of the VI "Real Time PID.vi", loop rates of (26 kHz) were achieved.

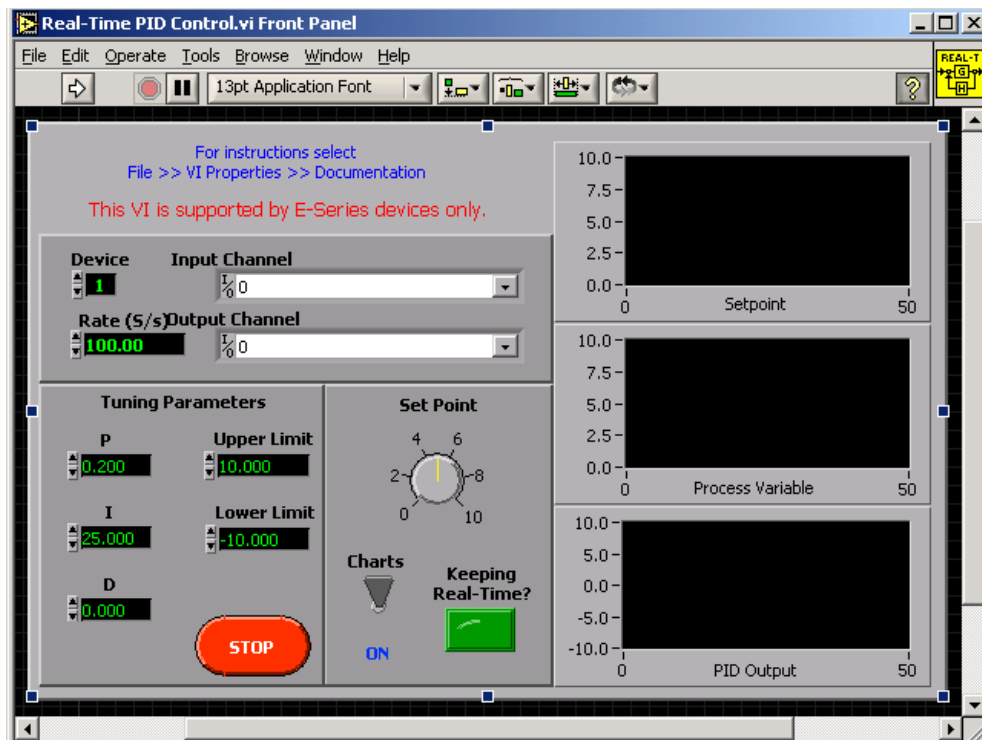


Figure 21. 'Real Time PID Control.vi' Front Panel. The user interface for 'Real-Time PID Control.vi'.

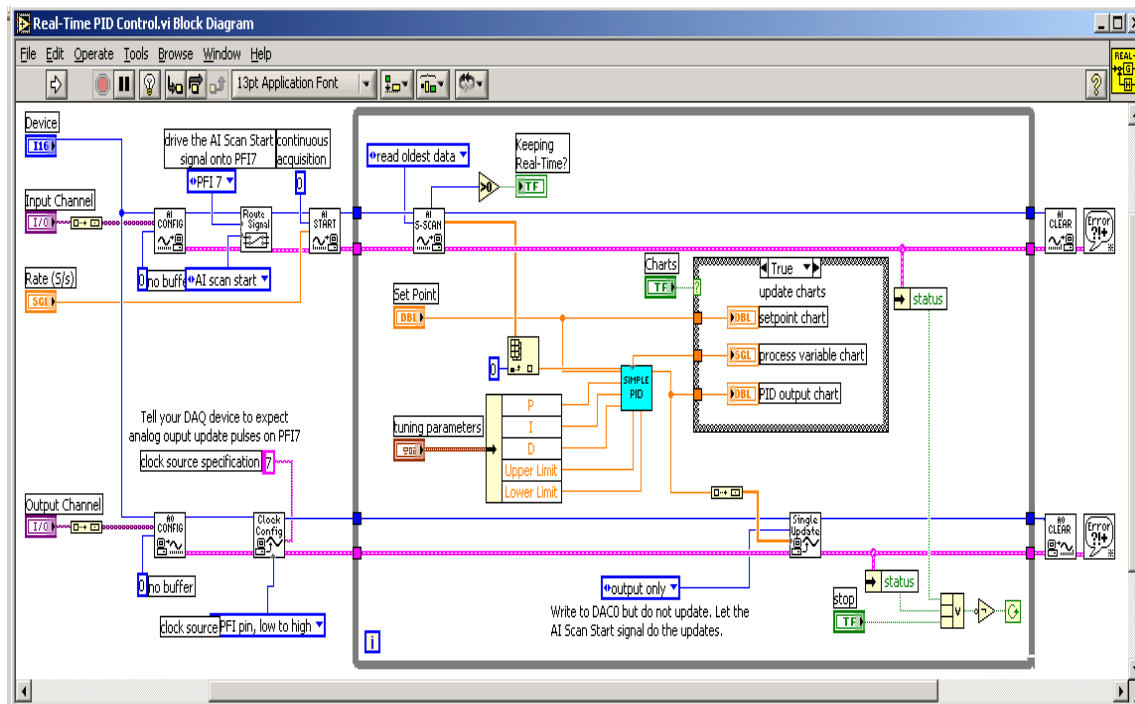


Figure 22. 'Real Time PID Control.vi' Block Diagram. The functional diagram of 'Real-Time PID Control.vi'.

E. SERIES LC RESONANT CIRCUIT SIMULATION

The LabVIEW based data acquisition system was implemented as the controller based on previous research by Fiorani (2002), who utilized a three axis kinematic PZT mirror mount and an operational amplifier (opamp) based controller. It was found that the PZT mirror mount provided adequate displacements to measure the vibrations, but the displacements were small enough that the noise generated by the circuitry in the controller contributed significantly to the data. For this research, the opamp-based controller could have been implemented for the larger displacements of the loudspeakers in the physical model system. However, for the time savings and ease and accuracy of adjusting the controller gains and feedback characteristics, LabVIEW was chosen for the controller.

Two versions of the LabVIEW Virtual Instrument (VI) controllers were implemented in the research, one contained a PD (proportional and derivative) feedback loop along with a white noise generator while the other only contained a PD feedback loop. The version with the white noise source was used for the equivalent electrical circuit. The controller with the PD feedback loop, which is shown in Figs. 23 and 24, was used for the physical model system. Both VI's had the capability to show both the signal at the input and output of the controller, although the loop rate was reduced from 20,000 samples per second to 13,000 samples per second with the graphs displayed.

The series LC resonant circuit was designed to be the electrical equivalent of a single-degree-of-freedom mechanical oscillator and allow verification of the LabVIEW controller operation. The circuit contains an inductor representing the mass of the oscillator, a capacitor representing the stiffness, an AC voltage source representing the noise drive $[F(t)]$ and an AC voltage source representing the control drive $[-G(x, dx/dt)]$ in series and shown in Fig. 25. By measuring the voltage across the capacitor, the displacement of the vibrating strip could be measured and then reduced by the active control system.

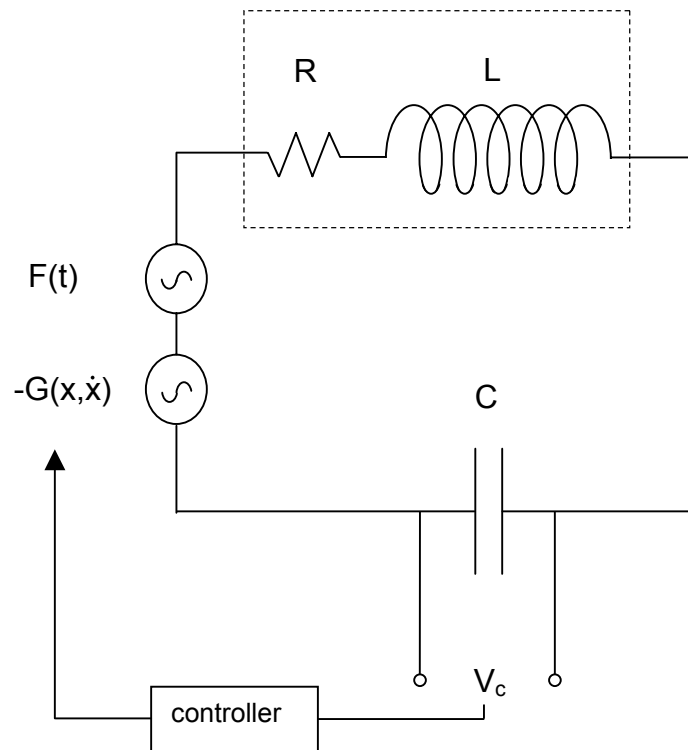


Figure 25. **Electrical equivalent circuit of physical model system.** The series LC circuit is represented along with the small internal resistance of the inductor.

The series LC resonant circuit was constructed using a $100.0\mu\text{F}$ capacitor, 5.725mH inductor with a small internal resistance of 2.95Ω . An HP 35665A dynamic signal analyzer was used for the swept sine frequency response measurements while LabVIEW was used to generate both the white noise drive and feedback control drive during the control portions of the experiment. The calculated resonance frequency of the circuit was 184Hz while the measured

resonance frequency was 180 Hz. A plot of the frequency response from the swept sine measurements is shown in Fig. 26.

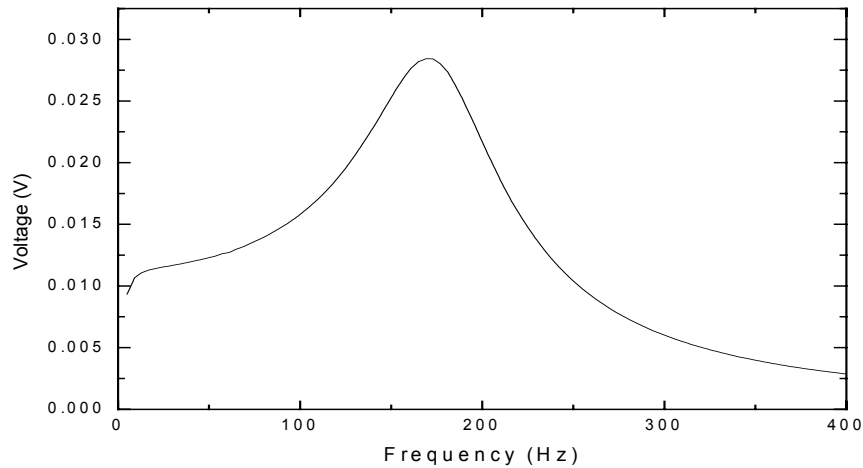


Figure 26. **Series LC resonator frequency response.** The swept sine frequency response of the series LC circuit obtained using an HP 35665A dynamic signal analyzer.

While conducting the swept sine frequency response measurements, the system showed signs of nonlinearity. As the drive amplitude was increased, the resonance frequency decreased. For drive amplitudes up to 5mV, the resonance frequency remained within 5 percent of the theoretical value and it was believed that if the drive amplitude remained below this level, tests of the circuit using the control system would avoid the nonlinear characteristics of the circuit.

The effects of the circuit due to the control circuit for both proportional and derivative were then investigated. According to the theory developed in Chapter II, when the proportional gain α is increased, the stiffness of the system will increase causing the resonance frequency to increase as well. The results of increasing the proportional gain caused the resonance frequency of the circuit to increase as shown in Fig. 27 for increasing values of α .

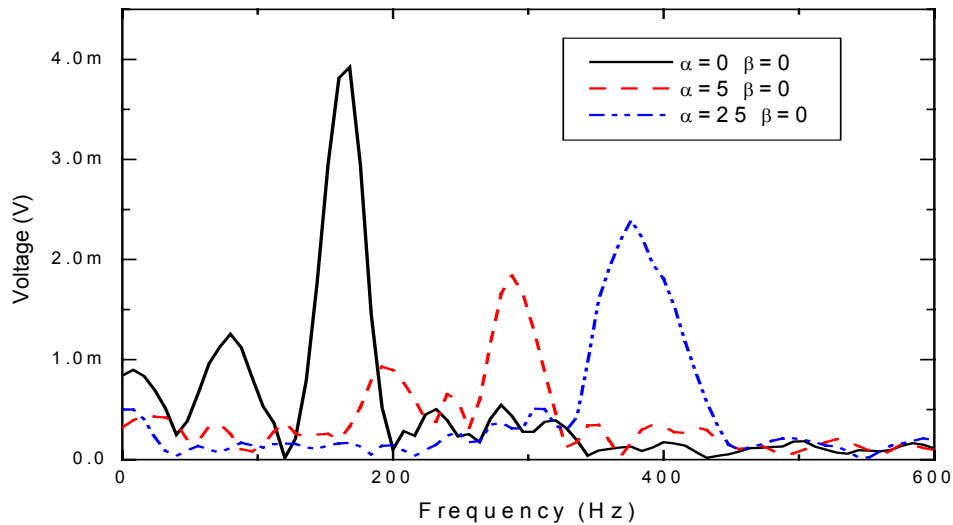


Figure 27. **Plots of increasing proportional gain.** The frequency response plots of the series LC circuit when driven with white noise from the LabVIEW controller are shown for increasing amounts of proportional gain.

For increased values of derivative gain β the damping of the system will increase and the amplitude at the resonance frequency will then decrease. This trend is shown in Fig. 28 for increasing values of β . Although the plots are not as clean as we expected, the general trends can be distinguished with one exception. In Fig. 27, the amplitude should steadily decrease for increasing values of α . This did not occur and is attributed to the oscillations in the response influencing the amplitude at the resonance. The oscillations that occur in both Figs. 27 and 28 are believed to be a result of the nonlinear response of the inductor core reacting to the noise drive. Due to these oscillations we did not continue with a ganging of the gains for a combined PD controller. A source of future work would be to replace the inductor used in this circuit with one that has a more linear response and replotting the data shown in Figs. 27 and 28 and then continuing with the theory and plotting the effects of ganging the gains.

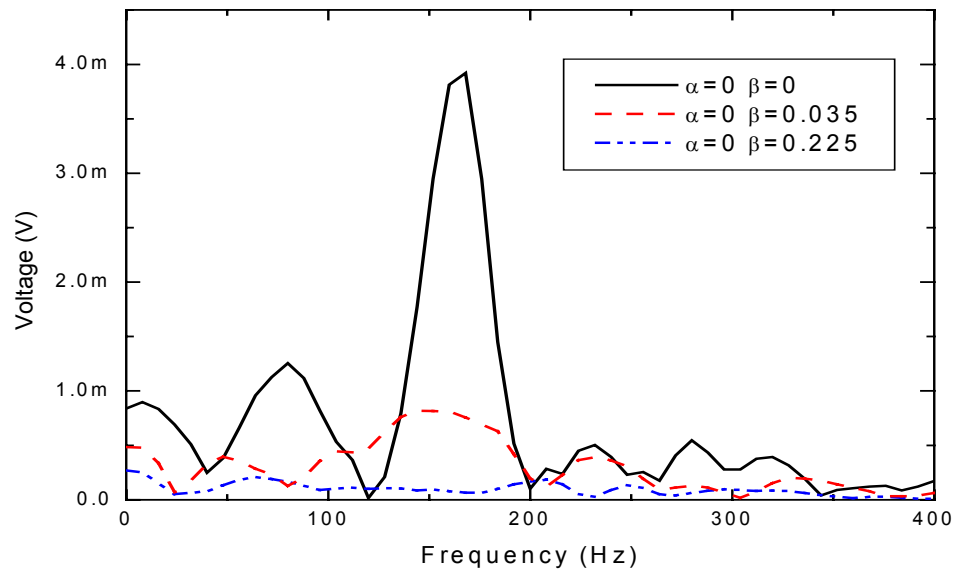


Figure 28. **Plots of increasing derivative gain.** The frequency response plots of the series LC circuit when driven with white noise from the LabVIEW controller are shown for increasing amounts of derivative gain.

THIS PAGE INTENTIONALLY LEFT BLANK

V. ACTIVE VIBRATION CONTROL EXPERIMENTS

The purpose of the physical model system is to experiment with it in order to understand the underlying physics of active feedback control, and to show a visible demonstration of the effectiveness of active control.

A. APPARATUS

The apparatus employs the same basic optical detection method as the apparatus of Fiorani (2002), however, the 3 axis kinematic PZT mirror mount has been replaced with a clamped flexible strip driven by two loudspeakers as diagrammed in Fig. 29. A mirror is mounted to the flexible strip allowing the reference diode laser to transduce the motion of the flexible strip to a quad photodiode that acts as a position sensing detector (PSD). The strip is designed to be flexible only in the horizontal plane and rigid in all other directions. The control circuit includes the standard PD (proportional-differential) control components. Most control systems also include an integral control. However, the theory presented in Chapter II does not indicate a need for this type of control, and so it has not been included here. For the demonstration system, the user will be able to vary the proportional and derivative gains of the controller and observe how these affect the vibrations of the system.

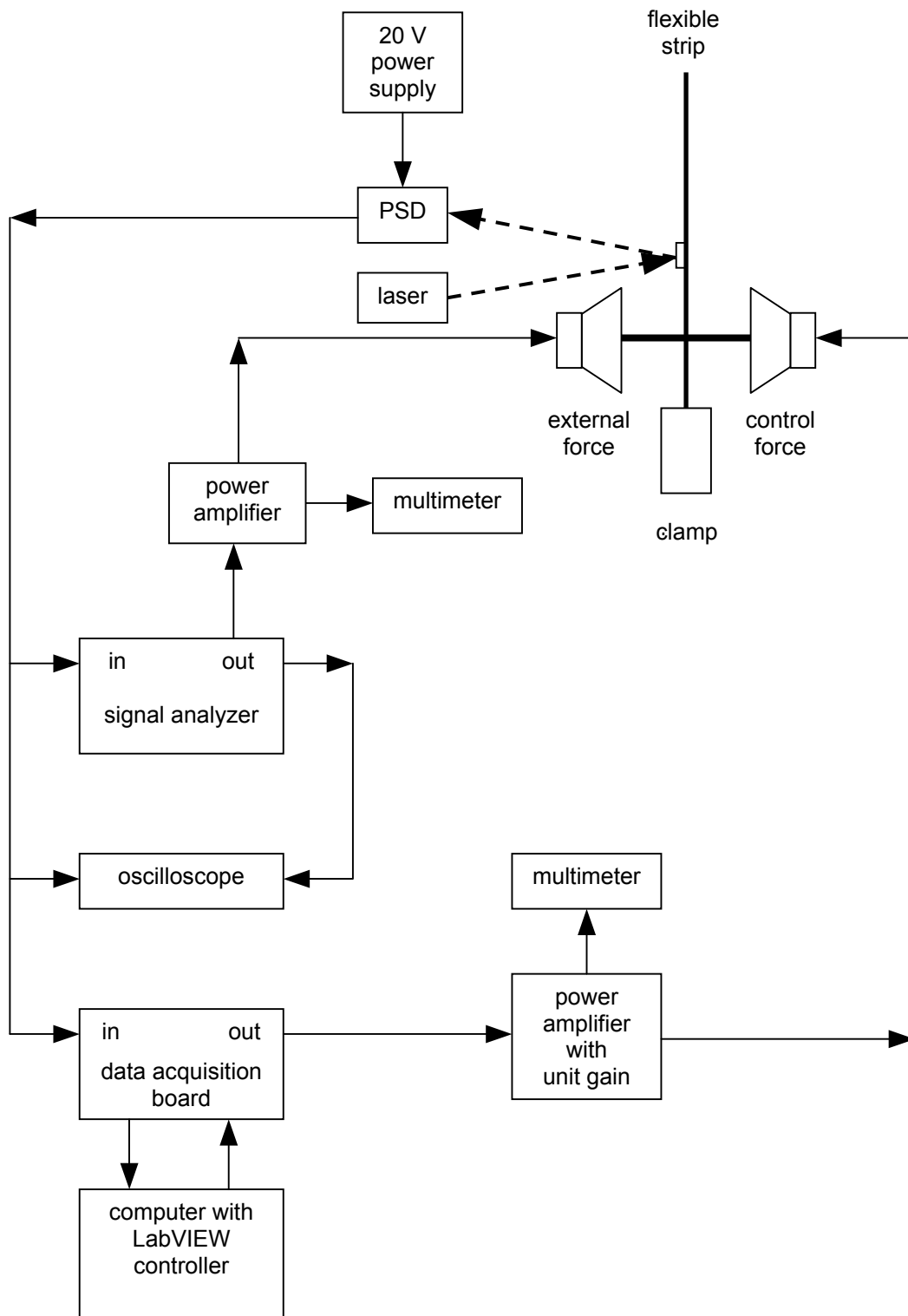


Figure 29. **Diagram of experimental apparatus.** The out terminal of the signal analyzer can be replaced with a function generator.

The detection system includes a reference diode laser (Thorlabs S2011), a half inch square mirror (Thorlabs ME05S-GO1) and a quad photodiode (Pacific Silicon Sensor QP50-6SD). The reference diode laser is a complete kit that includes a focusable diode laser, an adjustable mount and the power supply. The mirrors are front surface economy mirrors chosen to allow permanent bonding to the vibrating strips being tested. The quad photodiode contains four quadrants on its face and provides top minus bottom and left minus right difference signals from self contained circuitry. Although this would allow for two dimensional alignment, we used only a single dimension in this research. The detector ambient light voltage response is shown in Fig. 30 and shows that for our detection system we have approximately 4mV of noise. This noise was overcome by using the loudspeakers which provide displacements that are at least two orders of magnitude greater than the noise.

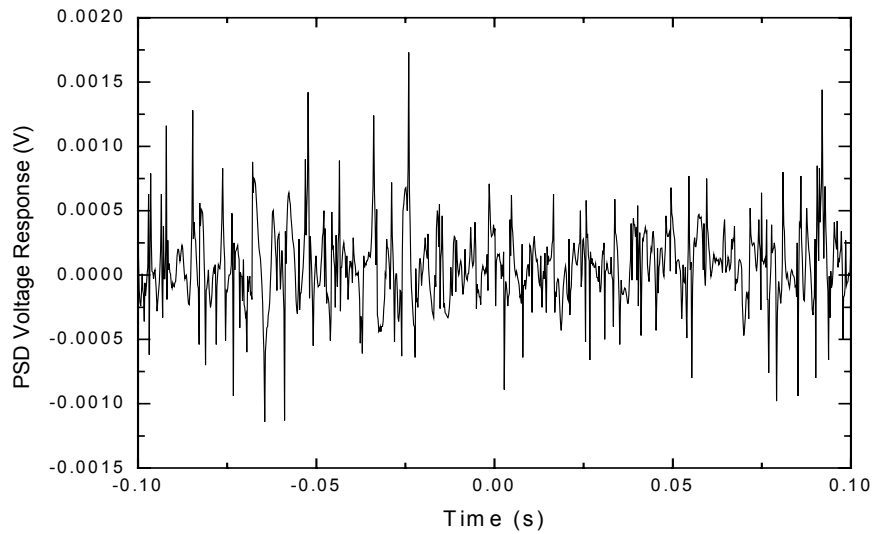


Figure 30. **PSD ambient light response.** Time series response of the quad photo detector used to determine the noise level in the electronics and ambient light.

The flexible strip and clamp were designed to constrain vibrations to a single plane of motion and roughly approximate the motion of a clamped-free

bar. The clamp was machined from an aluminum I-beam with base dimensions of five inches by three inches and 1/4" thickness. The top of the I-beam was removed for visibility of the apparatus and the cross section of the clamp thus appears as an inverted 'T' as shown in the photograph in Fig. 31. The strip in the experiment is a 16.2" long by 3/4" wide by 1/16" thick aluminum strip. The flexible strip is 9.6" in length from the rigid clamping point to its free end and is driven one inch from the edge of the clamp. The mirror used to transduce the motion of the flexible strip is 4 inches from the drive point (five inches from the edge of the clamp).

The actuator system chosen for both the noise drive and control drive are four inch electrodynamic loudspeakers. These drivers were chosen over piezoelectric actuators for many reasons, one of which is to dominant the ambient noise of the environment the system will operate in since the major focus of this research is to probe and demonstrate the effects of active control systems. The loudspeakers also produced sufficient displacements of the strip so that the standing wave pattern of each mode could be felt by hand. This identification of the modes is critical for our understanding of the behavior of the feedback. Loudspeakers also allow the flexible strips to be interchanged without needing to have permanently affixed piezoelectric plates attached to all the test samples. This provides for a more cost effective apparatus keeping in mind the goal of a demonstration model and for a more visible demonstration. The electrodynamic loudspeakers used were Morel MW113 4" vented woofers (specifications in Appendix C). Each loudspeaker is rigidly mounted using milled I-beams similar to the flexible strip clamp. The loudspeakers face each other and are connected through a 10-32 stainless steel threaded rod with the flexing strip mounted midway between the two loudspeakers as shown in Fig. 31.

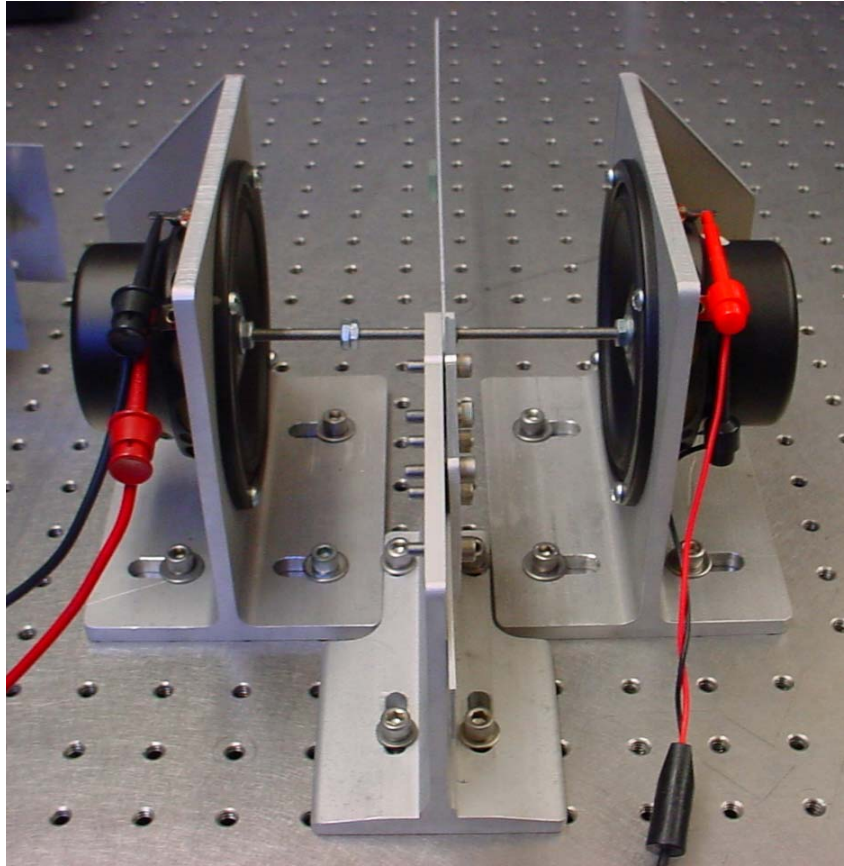


Figure 31. **Loudspeaker Mounting and sample vibrating strip.** The milled I beams are shown with the drivers mounted to the threaded rod and a thin sample vibrating strip between them.

The loudspeakers were attached to the stainless steel rod by Delron driver cups machined so their bases were the same radius as the driver dust caps shown in Fig. 32. This mounting scheme translates the loudspeaker motion through the rod attached to the flexible strip. Initially the driver cups were bonded to the loudspeaker dust caps by epoxy on the two surfaces. This secured the two components for a short period, after which the bond broke and left no trace of the epoxy on the dust cap. This problem was fixed with the aid of Wayne Prather (University of Mississippi) who recommended drilling small holes in the dust caps to allow some of the epoxy to seep through and bond to the rear of the dust cap. For future research, the two components could be mechanically bonded by utilizing the large diameter hole in the magnet of the vented loudspeaker. By drilling a through hole for the threaded rod in the driver cup and using a small

washer on the rear of the dust cap, the two components could be secured by lock nuts. A basic sketch of this mounting scheme can be seen in Fig. 33.

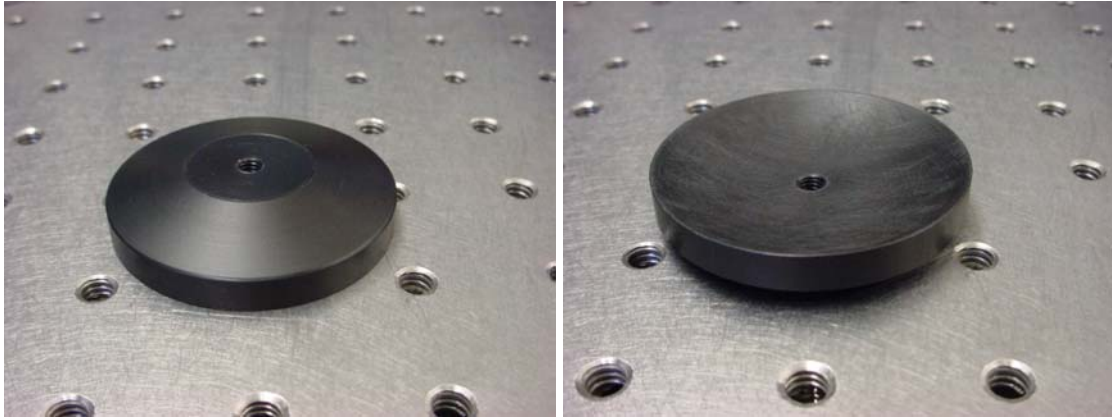


Figure 32. **Driver Cup.** The top of the driver cup is shown on the left and the bottom is shown on the right.

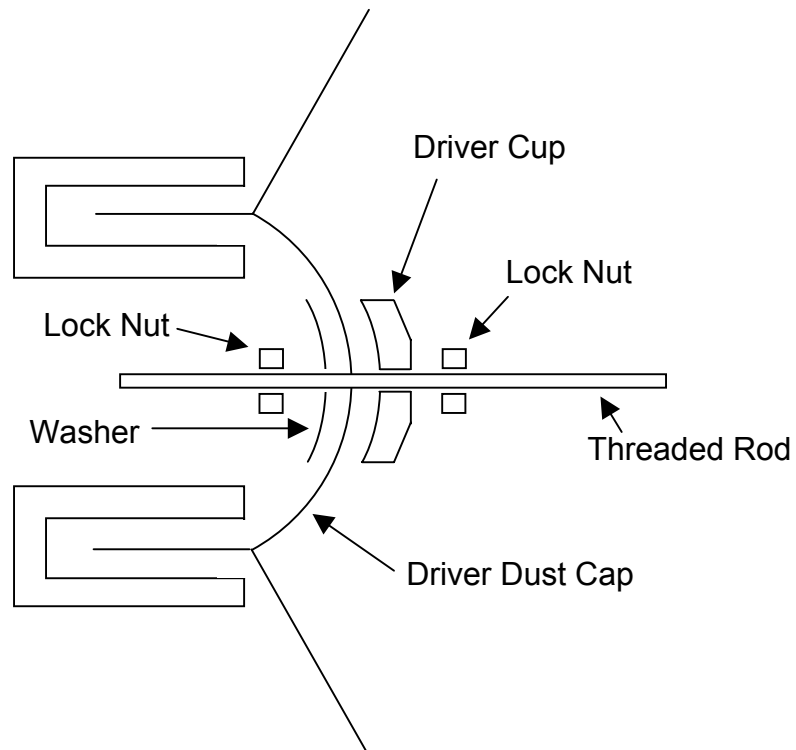


Figure 33. **Sketch of mechanical bonding of loudspeaker and driver cup.** This system can be used on vented loudspeakers only.

B. RESULTS

With the experimental apparatus constructed, the first measurement taken was to determine the frequency response of the system. Both swept sine (Fig. 34 (a)) and noise driven (Fig. 34 (b)) analyses were done, in order to verify that the results were the same.

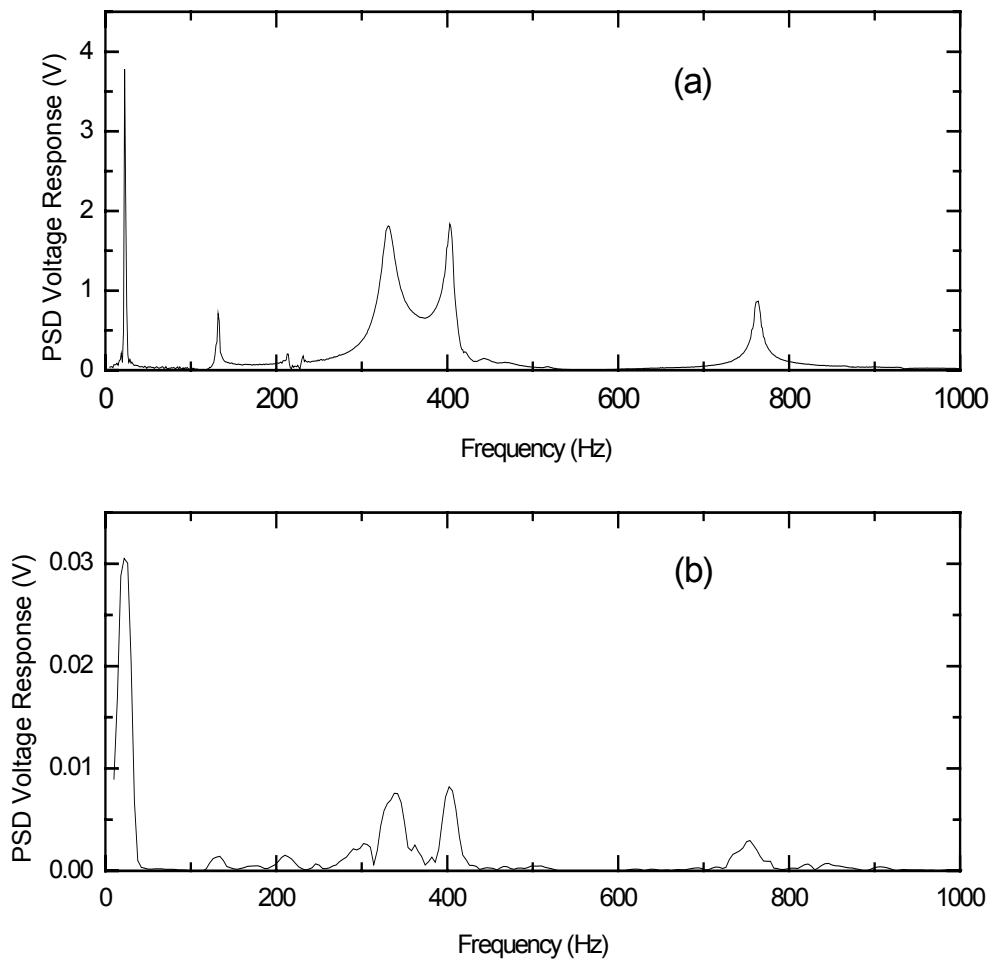


Figure 34. **Frequency response of physical model system.** Plot (a) is the swept sine frequency response driven at 0.10 VAC. Plot (b) is the averaged frequency response when driven with white noise.

Both response curves indicate modes of the physical model system at frequency values within experimental error. As displayed in Table 1, the first mode occurs at 22.2Hz and corresponds with the calculated fundamental mode of a clamped-free bar (Kinsler, et al., 2000). The remaining modes in the response curves are at 130.7, 225, 322.2, 399.0 and 761.8Hz. These modes were all verified to be the second through fifth flexural modes of the flexible strip with the exception of the 225Hz mode. The mode at 225Hz was found to be a result of vibrations in the driver mounts. By driving the system sufficiently hard, the mode structure of the flexible strip could be verified by feeling the location of the nodes. Although the theoretical modes of the system are much different above the third mode as shown in Table 1, the nodes of the flexible strip for the third mode and higher gravitate towards the mirror location due to the added mass of the mirror. The mass of the mirror was 50 grams and initially assumed to not have an effect on the mode structure but due to the differences noted in Table 1, that is an incorrect assumption. It also should be noted that the clamped end fails to be a node at higher frequencies.

Mode	Theoretical Frequencies (Hz)	Experimental Frequencies (Hz)	Phase (degrees)
1	22.7	22.2	-90
2	142.2	130.7	-90
3	398.2	322.2	+90
4	780.3	399.0	-90
5	1289.2	761.8	-90

Table 1. **Theoretical and experimental modes of the vibrating strip.** The theoretical modes represent calculations based on the vibrating strip behaving as rigid at the driving point and an approximate value for the speed of sound in aluminum. The experimental modes were determined from the swept sine and then driving the flexible strip at each frequency of interest to verify the mode. The phase -90° is the normal case of the displacement lagging the force by 90°.

1. Proportional Control

To initially observe the effects of the proportional control, the system was driven at a fixed frequency corresponding to the first mode of the system and plots were made of the PSD voltage response versus the proportional gain applied to the system. The proportional gain began at zero and was increased until the system became unstable (Fig. 35). The maximum reduction in the PSD voltage response prior to the system instability at 761.8Hz (fifth mode) was a factor of 16.

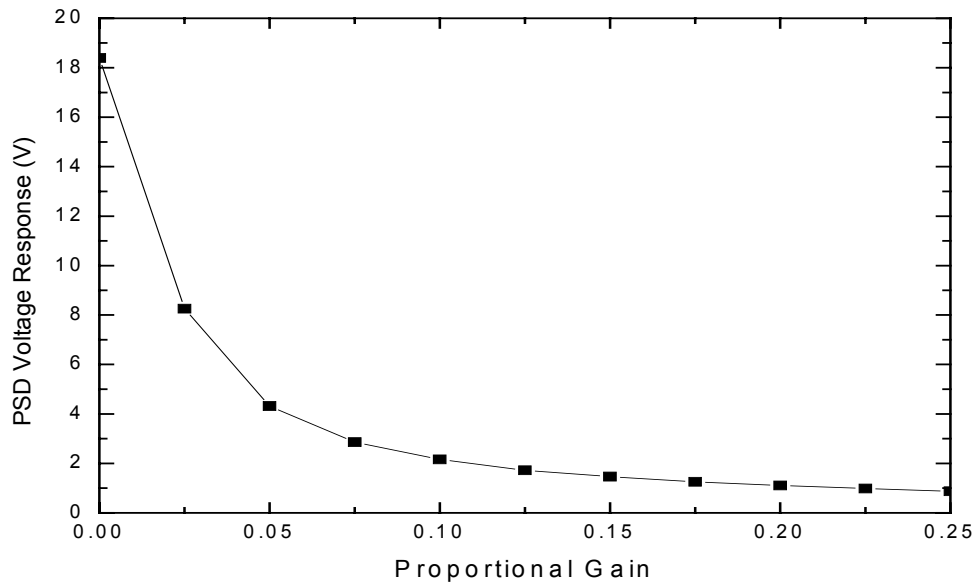


Figure 35. **Proportional (α) Gain Only.** The system was driven at 22.2Hz and the resultant PSD voltage response was measured for no gain and then increasing values of the proportional gain until the system became unstable.

In order to investigate the instability, zoomed in plots of the first, third and fifth modes were taken. The selection of these modes is significant since the fifth mode becomes unstable for large values of proportional gain and the third mode becomes unstable for large values of derivative gain. Fig. 36 shows that for increasing values of proportional gain with the derivative gain set to zero, the

resonance frequency of the first mode increases and the amplitude of the resonance decreases. This corresponds to the theory developed in Chapter II. Fig. 27(a) shows the system with no proportional gain and Fig. 36(c) shows the system with proportional gain just prior to the instability where there is an increase in resonance frequency of three percent and an amplitude decrease of 22 percent.

Fig. 37 shows the effect on the third mode, for the same increasing values of the proportional gains as in the first mode. It is important to note that the theory in Ch. II should apply here, even though it was developed for a single degree-of-freedom system, because the modes are uncoupled for small displacements. That is, the modes are *normal modes* for linear motion, so the theory should apply to each individual mode. The resonance frequency decreases because the placement of the mirror on the vibrating strip introduces a phase shift creating positive feedback (refer to Table 1). However, contrary to the theory, the amplitude decreases and the quality factor increases. The theory predicts that for a decreasing resonance frequency (i.e. decreasing stiffness in the system) the amplitude should increase and the Q should decrease.

The fifth mode is shown in Fig. 38, and once again is plotted for the same increasing values of the proportional gain. This mode can be seen to increase in resonance frequency for increasing proportional gain, as expected. However, in contradiction to the theory, the amplitude and the Q increase, leading to the instability. We have not yet been able to explain this behavior. An understanding is important because it will lead to alterations of the system such that a greater gain is allowed before the instability occurs, which will cause greater stabilization.

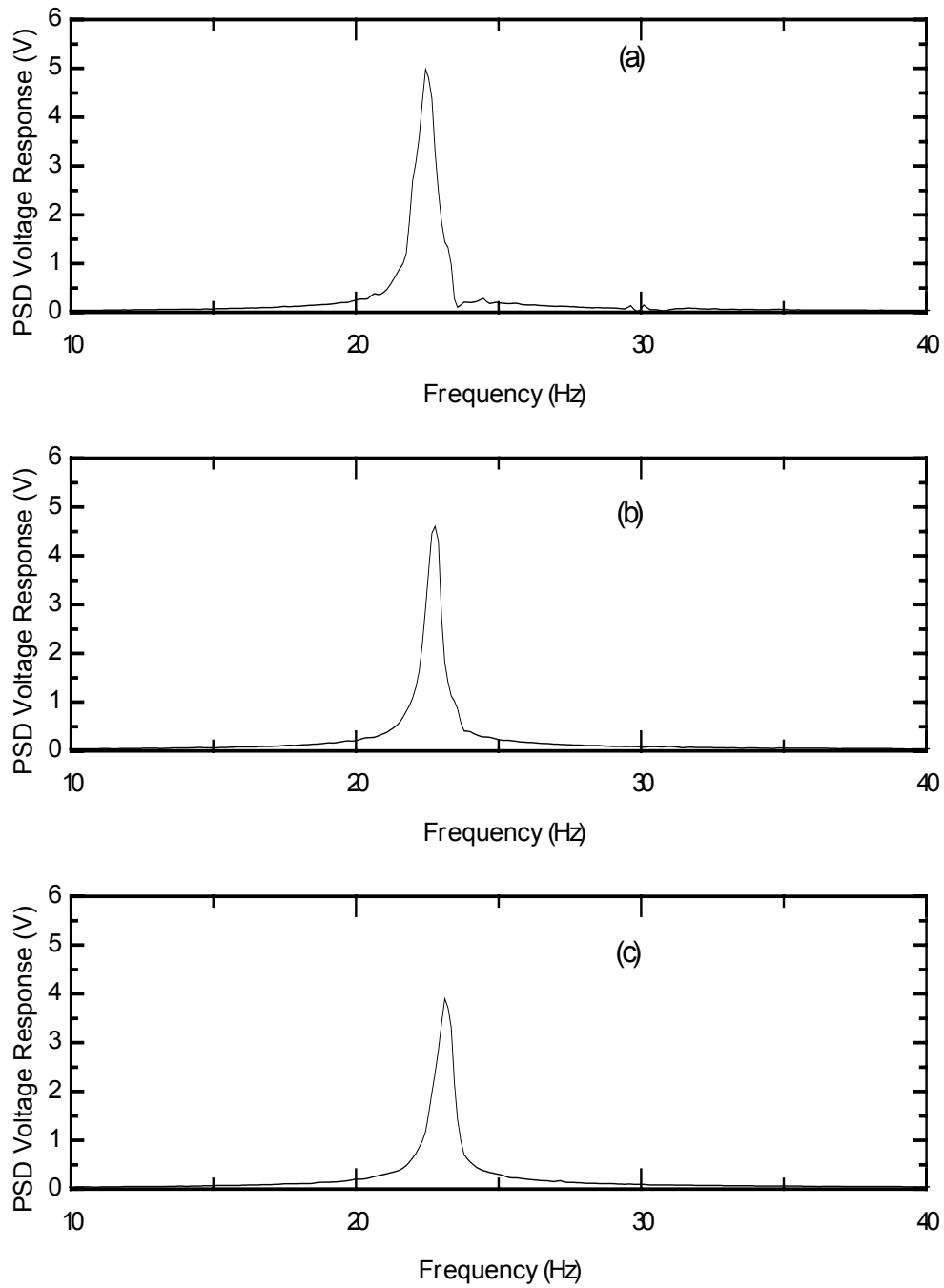


Figure 36. **Effects of increased proportional gain on the first mode.** The proportional gain α is (a) 0.0, (b) 0.06, and (c) 0.125.

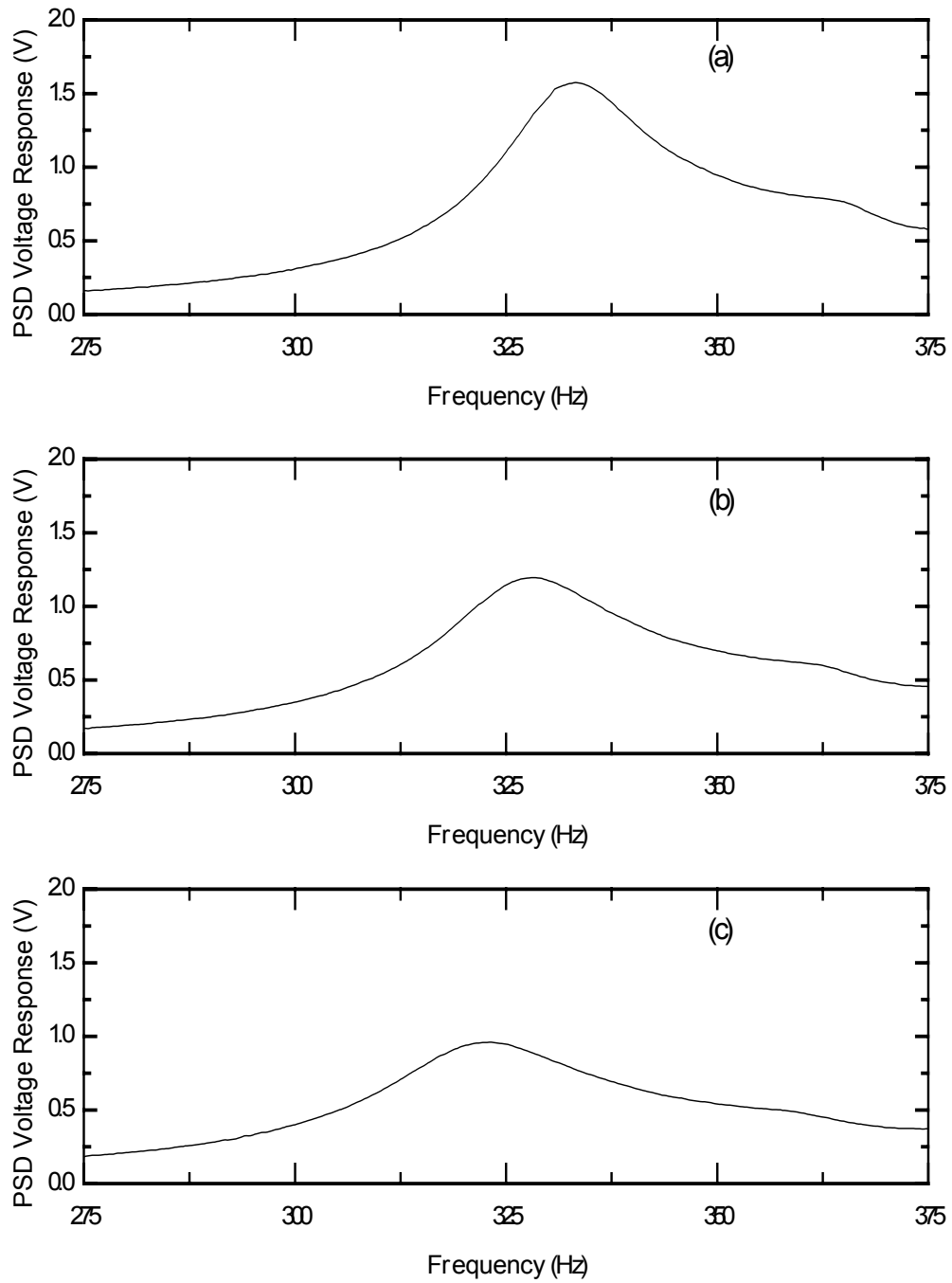


Figure 37. **Effects of increased proportional gain on the third mode.** The proportional gain α is (a) 0.0, (b) 0.06, and (c) 0.125.

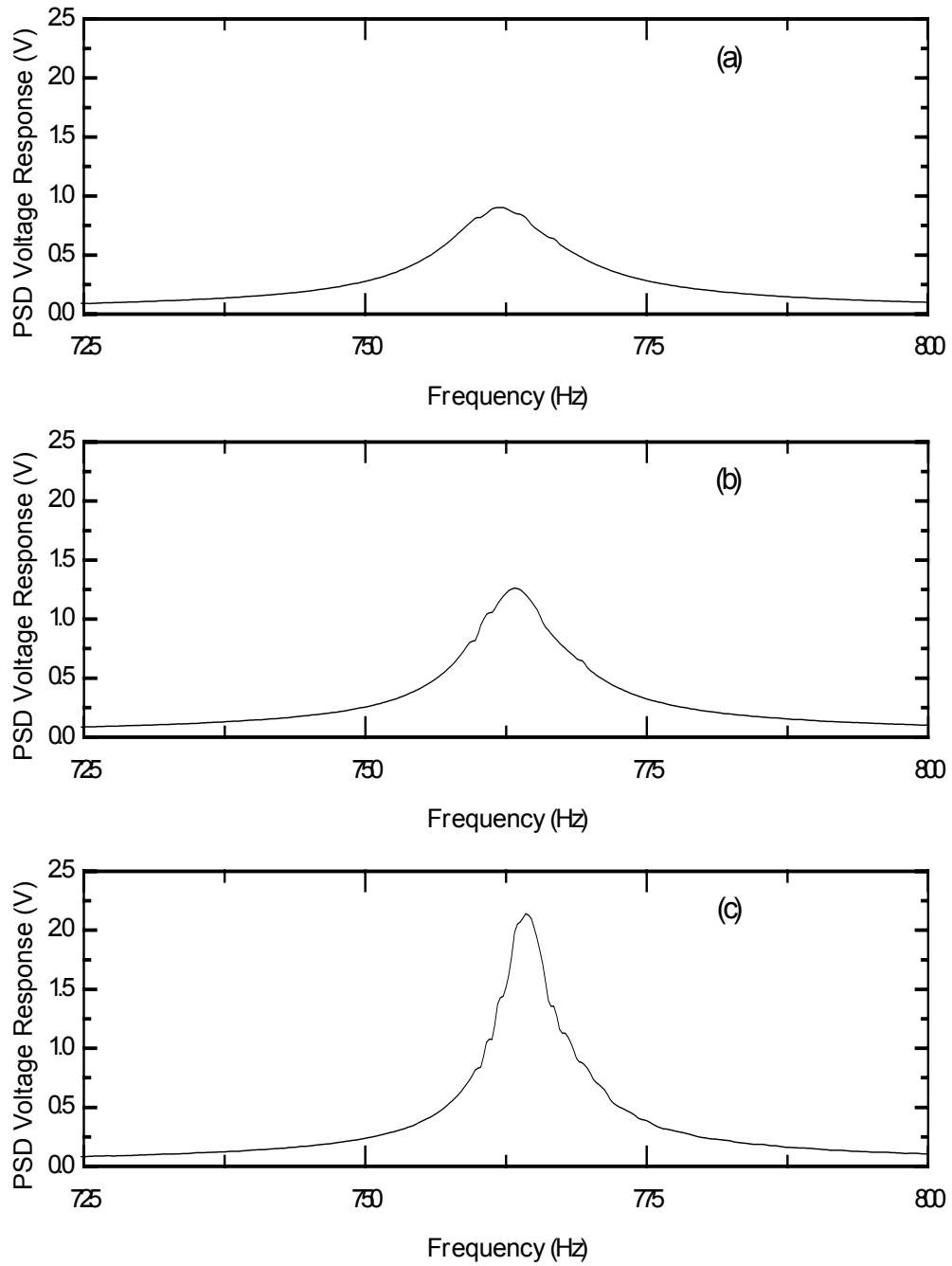


Figure 38. **Effects of increased proportional gain on the fifth mode.** The proportional gain α is (a) 0.0, (b) 0.06, and (c) 0.125.

2. Derivative Control

The effects of the derivative control were investigated similar to the proportional gain described in Section 1. A plot of the PSD Voltage response versus the derivative gain for fixed drive frequency is shown in Fig. 39. The maximum reduction with derivative control prior to onset of instability at 322.2Hz (third mode) is approximately a factor of 1.5.

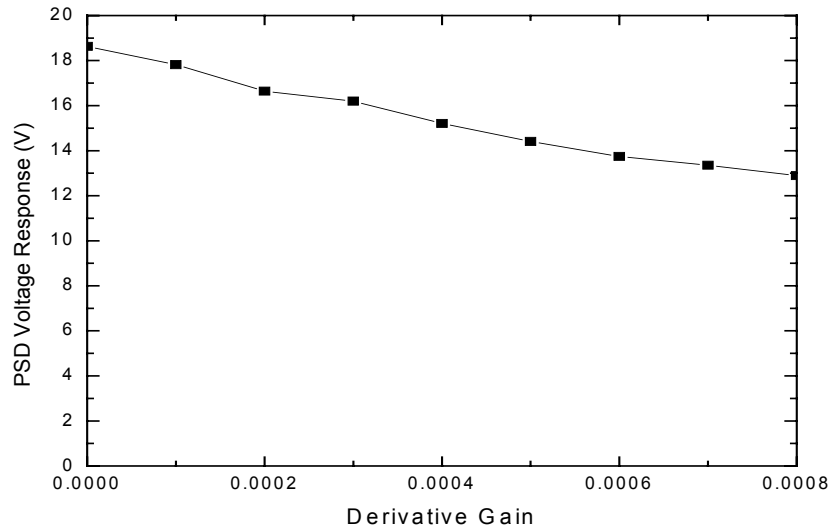


Figure 39. **Derivative (β) gain only.** The system was driven at 22.2Hz and the resultant PSD voltage response was measured for no gain and then increasing values of the derivative gain until the system went unstable.

To probe the instability of the system, we zoomed in on the first, third and fifth modes of the system as described earlier. The results of the first mode are shown in Fig. 40 for increasing values of the derivative gain while the proportional gain is set to zero. For the three modes, the graphs show derivative gains of (a) zero, (b) 0.0002 and (c) 0.00045. As expected from the theory, the first mode shows that the resonance frequency remains the same while the amplitude decreases for increasing values of the derivative gain. This effect corresponds to increasing damping in the system provided by the derivative gain.

The third mode shown in Fig. 41 grows in amplitude due to the positive feedback as in the proportional experiment. In the current case, this feedback leads to the instability. Surprisingly, the results now clearly reveal a softening nonlinearity [Fig. 41(c)], even though the response amplitude appears to be small. For increasing values of the derivative gain, the resonance frequency decreases due to the nonlinearity.

The fifth mode shown in Fig. 42 also exhibits the characteristics of a softening nonlinearity, although the effect is not as great. For this mode, the resonance frequency increases and the amplitude decreases. Once again the theory predicts the resonance frequency should not shift and the amplitude should decrease.

In our system, the maximum reduction in response amplitude that can be obtained with the proportional and derivative controls is small. We attribute this lack of substantial reduction to the high quality factors of the modes that become unstable as the proportional and derivative gains are increased. The high quality factors cause the instabilities to occur for small values of the gains, which limits the effectiveness of controls. High quality factors are common for simple systems of flexing bars. More complicated systems such as mirror mounts typically have lower quality factors, which was the case in the experiment of Fiorani (2002). One means of improving the reduction in amplitude in our system would be to increase the damping, for example, by putting a piece of rubber in contact with the flexing strip. Another means would be to low-pass filter the signal from the position detector to the control circuit, which is commonly done in control systems such as those for laboratory free-electron laser mirrors. This is effective because the modes that become unstable occur at higher frequencies. By filtering the signal at these frequencies the feedback becomes positive only at much larger values of the gains, so a substantially greater reduction of the lower-frequency response is obtained.

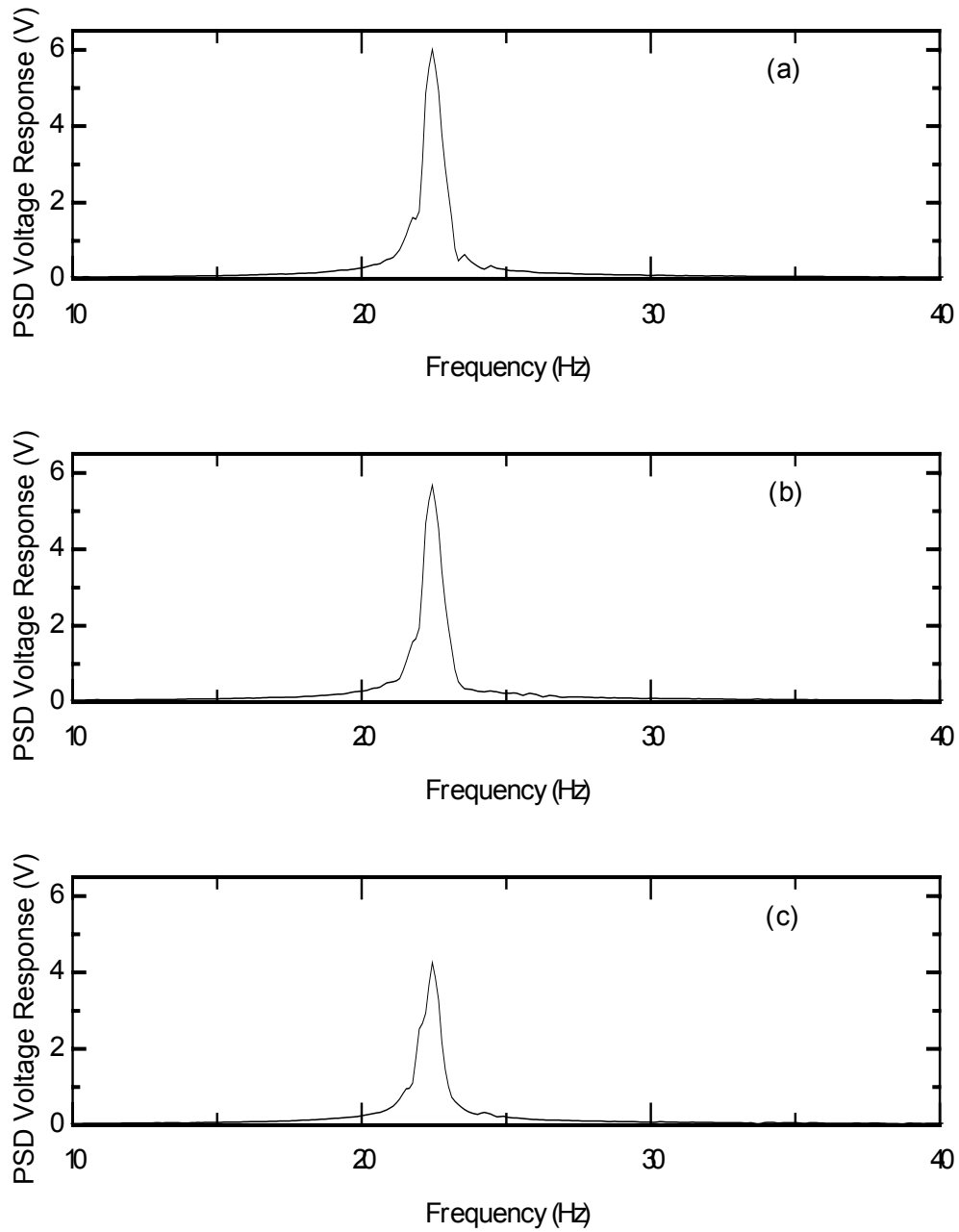


Figure 40. **Effects of increased derivative gain on the first mode.** The derivative gain β is (a) 0.0, (b) 0.0002, and (c) 0.00045.

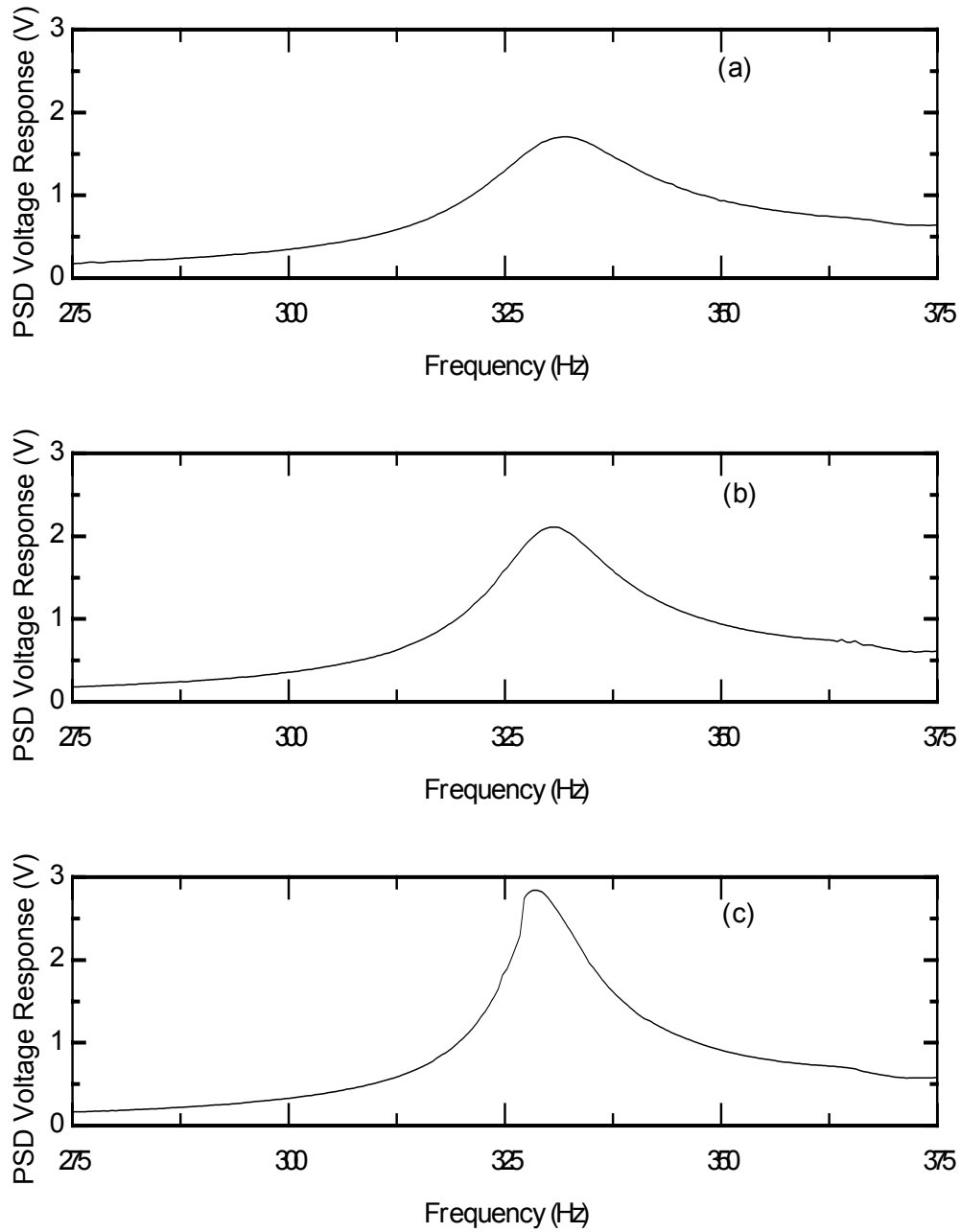


Figure 41. **Effects of increased derivative gain on the third mode.** The derivative gain β is (a) 0.0, (b) 0.0002, and (c) 0.00045.

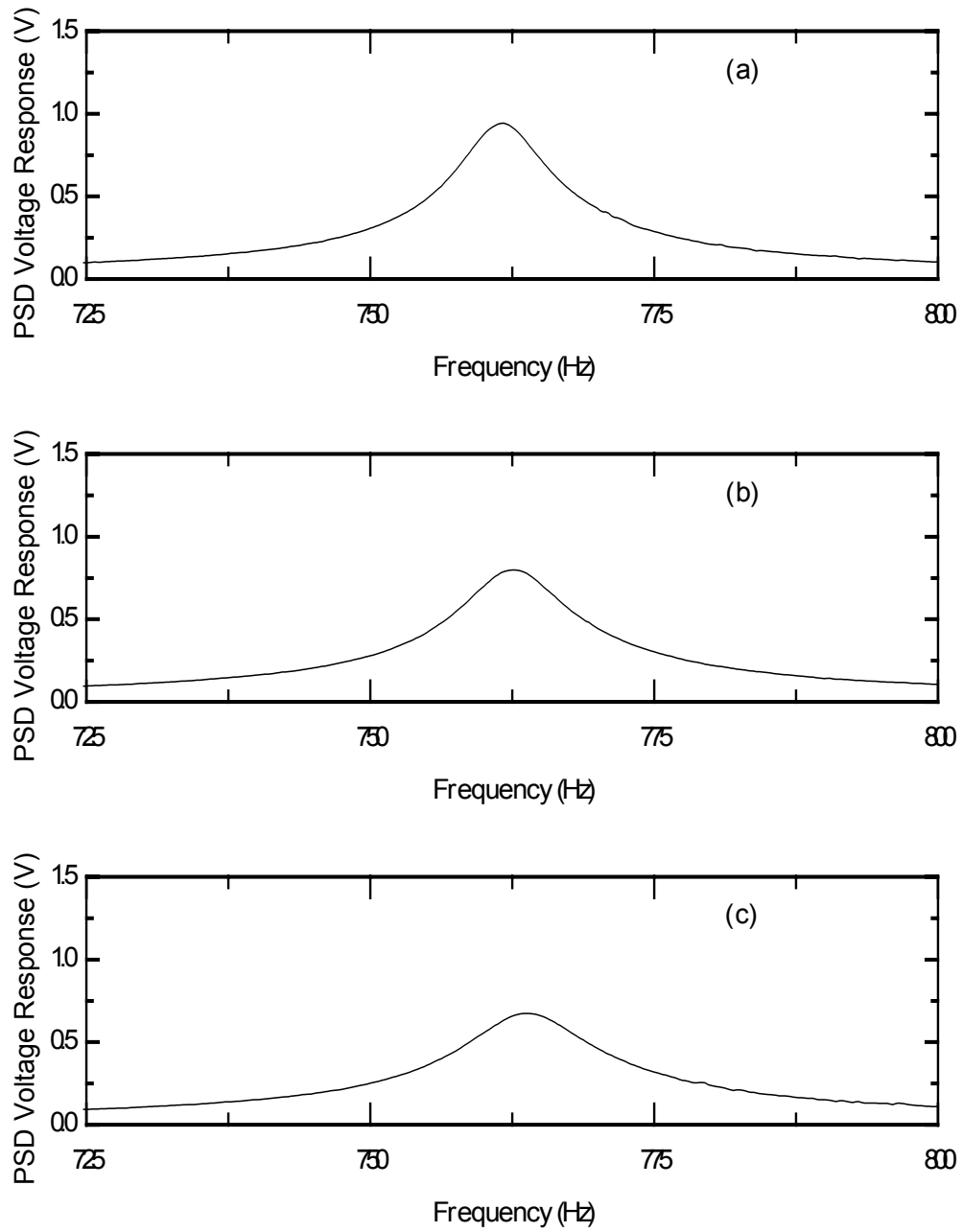


Figure 42. **Effects of increased derivative gain on the fifth mode.** The derivative gain β is (a) 0.0, (b) 0.0002, and (c) 0.00045.

VI. CONCLUSIONS & FUTURE WORK

A. CONCLUSIONS

A theory for the feedback reduction (or stabilization) of the motion of a single-degree-of-freedom oscillator was developed and confirmed with numerical simulations. The simulations showed that the response due to external noise can be made as small as desired by increasing the proportional and derivative control gains, which increase the effective stiffness and damping, respectively, of the oscillator. No positive feedback occurs in this system, so the gains can be arbitrarily large. In addition to confirming the theory, the numerical simulations are important as a first step in future numerical simulations of more-complicated systems.

A computer data acquisition system (LabVIEW) was implemented for use in an experiment of vibration stabilization. This system has the advantage of replacing many pieces of electronic equipment with software instructions that can be quickly implemented and altered. The replaced equipment includes the proportional and derivative feedback controls. The system was checked by having it stabilize the electrical current in an inductor-capacitor (LC) circuit that was driven by noise. This circuit is the electrical equivalent of a single-degree-of-freedom mechanical oscillator driven by noise.

For the experiment, a mechanical apparatus was constructed that is similar to a laser mirror mount, but which is simpler so that the behavior of the system due to feedback control could be understood. The system is a flexing aluminum strip that is clamped at one end and free at the other, and is driven at a point near the clamped end by two small loudspeakers that act as shakers. One loudspeaker is driven by noise or a pure tone, while the other is driven by the control circuit. The angular displacement of the strip at a point is detected by reflecting laser light off a small mirror attached at the point. This same method is used in the stabilization of laboratory free-electron laser mirrors, except that

small-displacement piezoelectric drivers are used. An advantage of our system is that the modes can be readily identified due to the simplicity of the apparatus and the capability of substantial drive amplitudes. Another advantage is that the external force drive can greatly exceed ambient laboratory noise, so that clean and precise investigations can be performed.

The first five modes of the system were determined by a swept-sine analysis for zero gains of the proportional and derivative controls, and the changes in the modes were then observed as the gains were separately increased to the point of instability (positive feedback). In each case, a specific mode of the system became unstable. The complexities of past systems prevented this identification. Understanding the instabilities is vital because it can lead to alterations that allow for greater control gains and thus increased stabilization. The instability due to the derivative control arises because the mode is phase shifted by 180° compared to the other modes, which occurs due to the location of the mirror in the standing wave pattern. Increasing the derivative gain thus decreases the damping of the mode to the point that the overall damping is negative, at which point the motion is unstable. The instability is thus in agreement with the theory. For the proportional control, a different mode becomes unstable. The mode stiffens as expected, but the amplitude increases rather than decreases, which is in fundamental disagreement with the theory. As the control gain is increased, the amplitude eventually diverges. Due to time constraints, we were unable to understand the reason for this instability.

B. FUTURE WORK

The theory and experiments in this thesis will lead to a further understanding of the active stabilization of laser mirrors. The next task is to understand the instability due to the proportional gain. This can be probed by observing the effects of changes in the apparatus, for example, moving the mirror

on the flexible strip to different locations of the modes and thereby avoiding the positive feedback. Another possibility is to increase the stiffness of the clamp and pressure plate holding the vibrating strip as well as the loudspeaker mounts by hogging them out of solid blocks of aluminum as opposed to the milled I-beams. As a parallel development, numerical simulations of a flexing strip subject to proportional and derivative controls could be readily performed. These simulations would undoubtedly offer a powerful tool in understanding the instability due to the proportional gain.

The understanding of the proportional control instability, with the current understanding of the derivative control instability, will allow the system to be modified such that a much greater degree of stabilization can be achieved. Possible modifications include increases of passive damping and stiffening, altering the point of detection, and low-pass filtering the displacement signal before it is sent to the control circuit. In addition, the effect of the integral control can be investigated and included if it is found to be effective.

The apparatus can then be repackaged in a smaller footprint as a demonstration model and laboratory experiment. The proportional and derivative controllers should be implemented in hardware-based opamp circuits as opposed to use of LabVIEW, which will save both per unit cost and space.

The next step is to conduct a feasibility study for the possible implementation of a free-electron laser as a shipboard weapon system. This study will require gathering vibration data of ships and determining if existing control systems can reduce these vibrations to current operating specifications of an FEL, which are specified as mirror tolerances within $180\mu\text{rad}$. Our work with the laboratory experiment will be indispensable in the ultimate implementation of a shipboard FEL weapon for several reasons. A physical understanding of the nature of control instabilities will lead to improvements in the design of the mechanical support structure of the FEL to allow for greater control gains, which will increase the stabilization. In addition, it is almost certain that the controls will have to be individually customized for each ship, as well as periodically adjusted.

Control engineers routinely perform such modifications without knowledge of the underlying physics. Our understanding of the sources of the control instabilities will substantially aid in this process. We are grateful to the Naval Sea Systems Command and Office of Naval Research for their appreciation and support of this effort.

APPENDIX A COMPUTER PROGRAM FOR NUMERICAL SIMULATIONS

Listed below is the computer program used to simulate the feedback control of a damped noise-driven oscillator (Ch. III). The program is in the C language.

```

/*****
                                control.cpp
This program simulates the position x(t) of a damped oscillator whose
mass is driven by a white noise force per unit mass f(t). A feedback
control force per unit mass g(x,x') is also applied. The equation of
motion is


$$x'' + 2\gamma x' + \omega_0^2 x = f(t) - g(x,x'),$$


where  $g(x,x') = x_{\text{gain}}\omega_0^2 x + 2v_{\text{gain}}\omega_0 x'$ .

The program uses the Euler-Cromer method.
*****/
                                parameter list
*****/

x, v          position and velocity of oscillator
t             time
f0            natural frequency of oscillator
w0, w0sq      natural angular frequency and square of natural frequency
gamma         damping parameter of oscillator
dt            numerical time step
points        total number of time points (integer power of 2)
noise(t)      noise force
amp           amplitude of noise force
control(x,v)  control force
xgain         dimensionless proportional (x) control gain
vgain         dimensionless derivative (v) control gain
*****/

#include <stdio.h>
#include <stdlib.h>
#include <math.h>
#include <time.h>
#define pi      3.14159265358979323846
#define rand_max 32767
#define seed    0
#define f0      1.0
#define dt      0.001

```

```

#define          npower          14
#define          xgain           3.0
#define          vgain           1.9

double noise(double time);
double control(double position, double velocity);
double w0, w0sq, gamma, noiseamp;
int timesteps;
void parameters();
void main()
{
    double t, x, v, xnew, vnew, force, accel;
    long int tcount;
    FILE *fout;
    fout = fopen("dataout.dat", "w");
    parameters();
    srand(seed);
    x = 0.0; v = 0.0;
    for (tcount = 0; tcount <= timesteps; tcount++)
    {
        t = tcount*dt;
        force = noise(t) - control(x,v);
        accel = -2.0*gamma*v - w0sq*x + force;
        vnew = v + accel*dt;
        xnew = x + vnew*dt;
        x = xnew;
        v = vnew;
        fprintf(fout, "%f \t %f \n", t, x);
    }
    fclose(fout);
}
/*****          end of main program          *****/

/*****          calculate parameters          *****/
void parameters(void)
{
    int n;
    long int timepoints, points[100];
    double amp[100];

    for (n = 0; n <= 25; n++)
    {
        points[n] = int(pow(2.0, n) + 0.0001);
        amp[n] = 100.0*pow(2.0, 0.5*float(n - 14));
    }
    timepoints = points[npower];
}

```

```

        noiseamp = amp[npower];
        timesteps = timepoints - 1;
        w0 = 2.0*pi*f0;
        w0sq = w0*w0;
        gamma = 0.1*w0;
        return;
    }

    /***** forcing functions *****/
    double noise(double time)
    {
        double value;
        value = rand()/(double)rand_max;
        return noiseamp*(value - 0.5);
    }

    double control(double position, double velocity)
    {
        double xterm, vterm;
        xterm = xgain*w0sq*position;
        vterm = vgain*2.0*w0*velocity;
        return xterm + vterm;
    }

    /***** end of program *****/

```

THIS PAGE INTENTIONALLY LEFT BLANK

APPENDIX B BASIC LABVIEW STARTUP STEPS

The following slides contain the steps to open LabVIEW, start the controller, and adjust the changeable parameters of the controller. First double click the National Instruments LabVIEW 7 icon to start the program which can be found in Fig. 43.

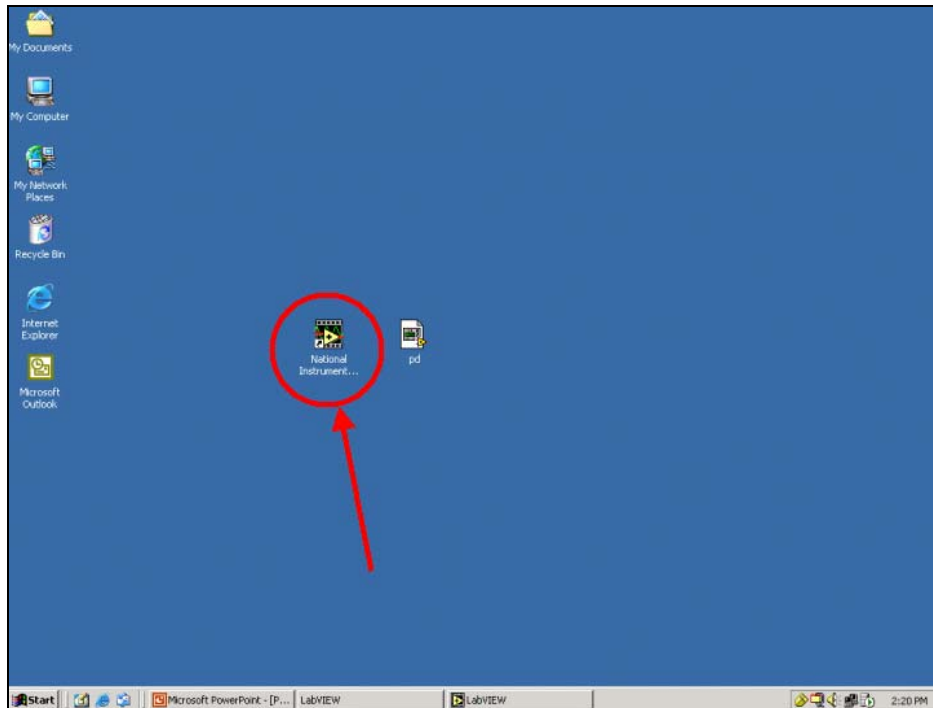


Figure 43. **Desktop following login.** This screen shows where the LabVIEW icon can be found to start the program.

Once LabVIEW has started, a small screen appears (Fig. 44) that allows some selections. The first will be to select RT:0, the DAQ installed in the computer, as the execution target. LabVIEW will then take a few seconds to connect to the DAQ, and then allow more selections to be made. Now we choose the 'Open...' button (shown in Fig. 45) which will open a window allowing selection of the VI to execute. Now select 'pd.vi' from the list of files on the desktop (shown in Fig. 46), this is our proportional and differential controller. In

order to run the VI, select the right facing arrow under the toolbar (shown in Fig. 47) to execute the VI. Once the VI is running, the values of the proportional and derivative gain can be adjusted as needed by highlighting the left or right most value (circled in Fig. 48) and typing a new value. To stop the VI from running, press the 'STOP' button.

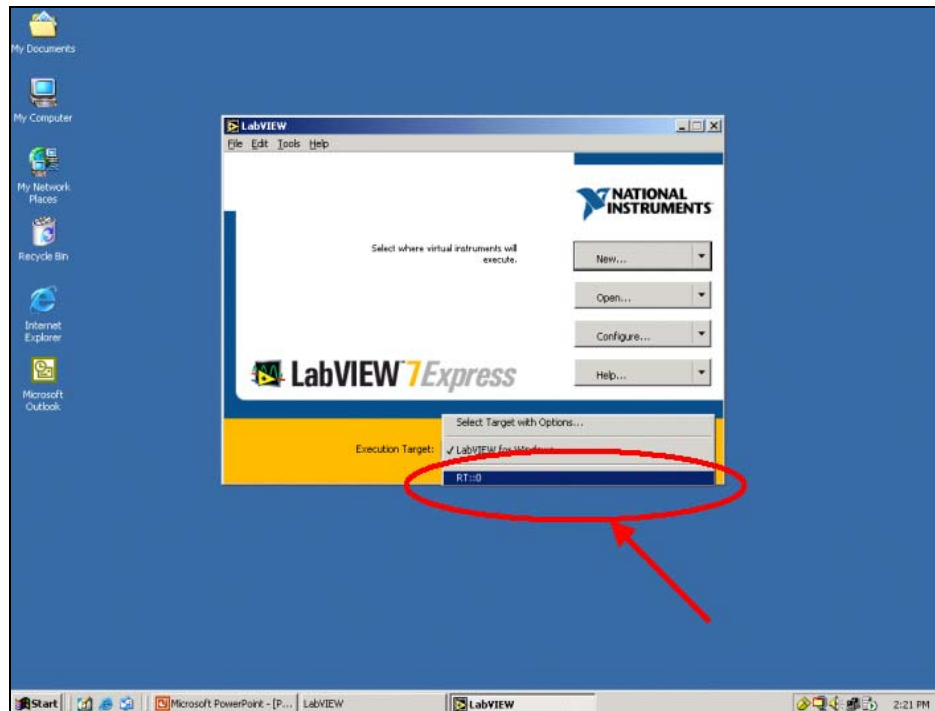


Figure 44. **Selection of the execution target.** Select 'RT:0' in order for the VI to be run from the DAQ instead of within Windows.

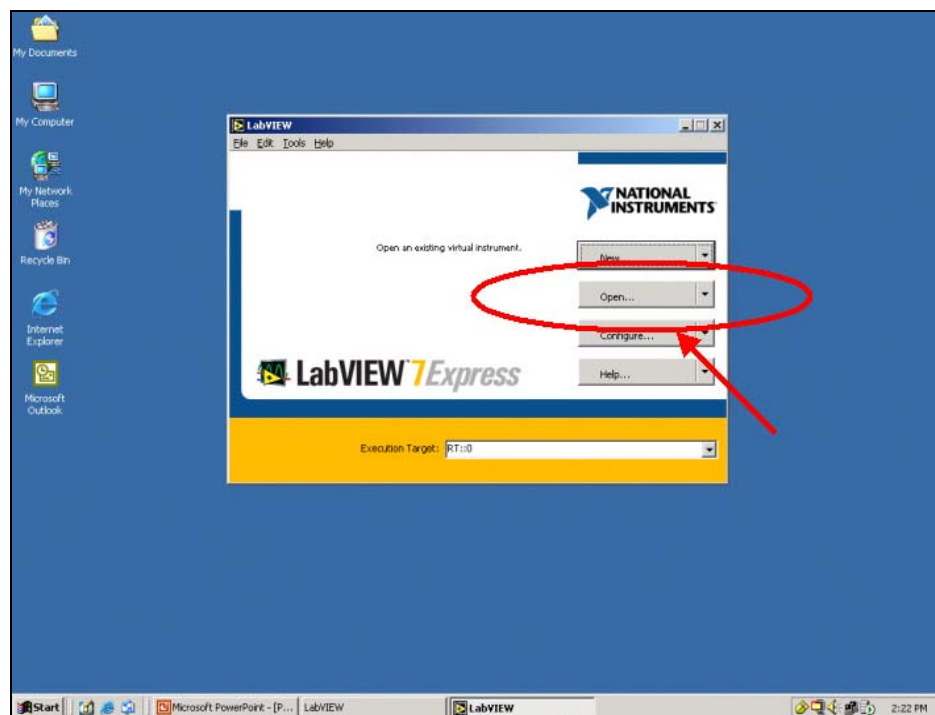


Figure 45. **Selection of the VI to open.** Select 'Open...' to open a window allowing the choice of the VI to execute.

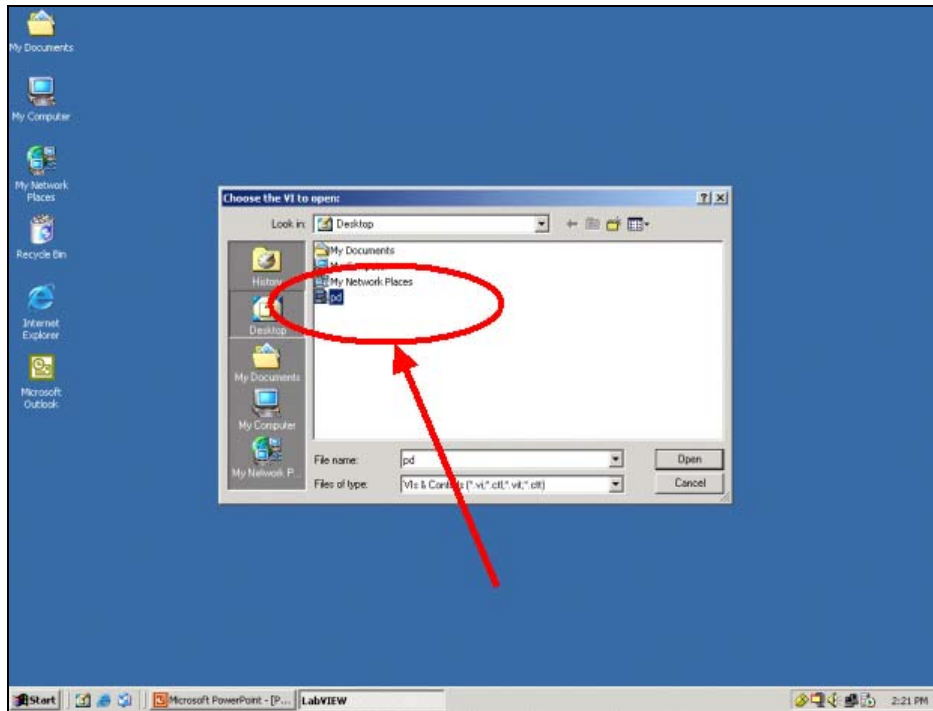


Figure 46. **Selection of 'pd.vi' as the controller.** Select 'pd.vi' from the list of files on the desktop to open the proportional and differential controller.

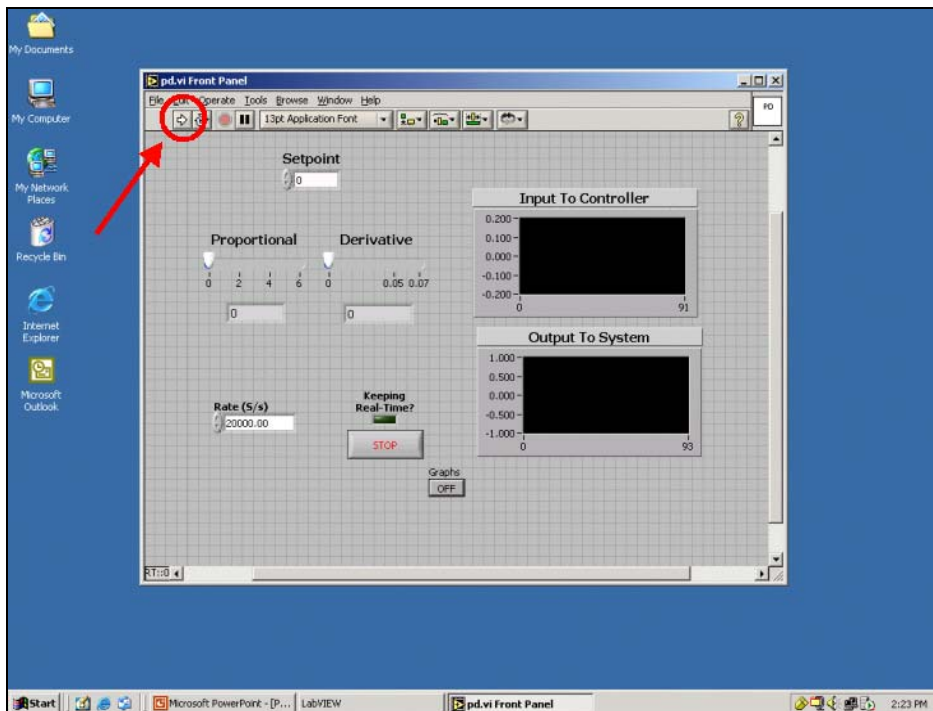


Figure 47. **Running the VI.** Click on the single right arrow under the toolbar to 'Run' the VI. This will download the VI to the DAQ (RT:0) for execution.

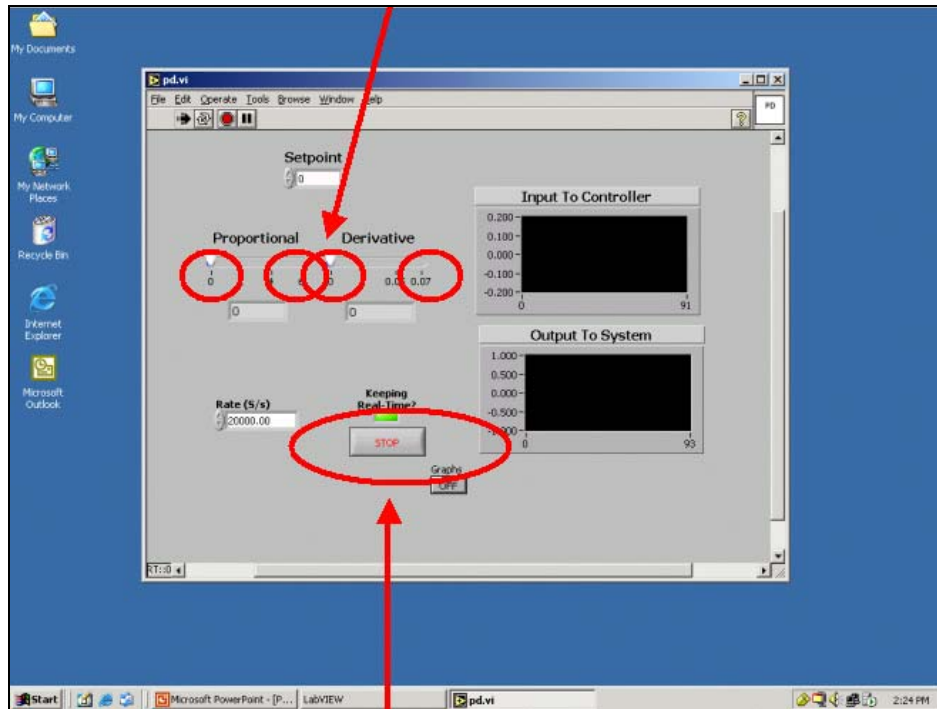


Figure 48. **Parameters on the controller and halting execution.** The left and right most values of the sliders can be changed to any desirable value. To stop the VI from running press, the 'STOP' button.

THIS PAGE INTENTIONALLY LEFT BLANK

APPENDIX C MOREL MW-113 LOUDSPEAKER SPECIFICATIONS

Application Information

Overall dimensions	118mm(4.64") x 58mm(2.29")
Baffle mounting hole diameter	95mm(3.75")
Nominal power handling	150W
Transient power - 10ms	800W
Nominal impedance	8 Ω
Sensitivity (1W/1m)	87dB
Frequency response	60-6,000Hz
Resonant frequency	72Hz

Voice Coil

Voice coil diameter	54mm(2.125")
Voice coil height	12.5mm(0.50")
Voice coil former	Aluminum
Voice coil wire	Hexatech Aluminum
Number of layers	2
DC resistance	6.2 Ω
Voice coil inductance	0.25mH

Magnet System

Magnet system type	Double magnet, vented
Magnet gap height	4.0mm(0.157")
Flux density	0.64T
BL product	3.98NA
Maximum linear excursion	±3.0mm(0.118")

Operational Parameters

Suspension compliance	844μM/N
Mechanical Q factor	3.13
Electrical Q factor	1.03
Total Q factor	0.75
Mechanical resistance	-
Moving mass	5.54g
Equivalent Cas air load	4.30L
Cone/dome material	DPC Damped Polymer Composite
Effective piston area	53cm ²
Net weight	0.50Kg

LIST OF REFERENCES

Crooker, P. P., Campbell, T., Ossenfort, W., Miller, S., Blau, J., Colson, W., "A Study of the Stability of a High-Power Free Electron Laser Utilizing a Short Rayleigh Length," paper presented at the FEL 2002 Conference, Argonne, IL, September 2002.

Energen Inc. [<http://www.energeninc.com>]. (December 2003)

Fiorani, F.M., "Active Mirror Alignment for Free Electron Lasers", Master's Thesis, Naval Postgraduate School, Monterey, California, December 2002.

Freund, H. P. and Antonsen, T. M., *Principles of Free-Electron Lasers*, pp 1-5, Chapman and Hall, London SE1 8HN, UK, 1996.

Kelly, M., Energen, Inc, October 2003 (private communication).

Kinsler, L.E., Frey, A.R., Coppers, A.B., Sanders, J.V., *Fundamentals of Acoustics*, 4th ed., John Wiley & Sons, 2000.

Morel Acoustics USA, Inc, "MW-113 Specifications"
[<http://www.morelusa.com/midranges/mw113specifications.htm>].
(November 2003)

Prather, Wayne, University of Mississippi, November 2003 (private communication).

Todd, A.M., Colson, W. B., Neil, G. R., "Megawatt-Class Free Electron Laser Concept for Shipboard Self-Defense," *SPIE Proceedings*, v. 2988, pp 176-184, February 1997.

MIL-STD-167-1 Test Method Standard

OPNAVINST 9072.2, Shock Hardening of Surface Ships,
[<http://neds.nebt.daps.mil/>]. (November 2003).

Pacific Silicon Sensor, Inc., "QP50-6SD Data Sheet."
[<http://www.pacific-sensor.com/pdf/QP506SD.pdf>]. (November 2003).

University of Maryland, Institute for Research in Electronics and Applied Physics,
"What is a Free Electron Laser."
[<http://www.ireap.umd.edu/FEL/whatis.htm>]. (October 2003)

THIS PAGE INTENTIONALLY LEFT BLANK

INITIAL DISTRIBUTION LIST

1. Defense Technical Information Center
Ft. Belvoir, VA
2. Dudley Knox Library
Naval Postgraduate School
Monterey, CA
3. Physics Department
Naval Postgraduate School
Monterey, CA
4. Professor Bruce Denardo
Naval Postgraduate School
Monterey, CA
5. Professor Thomas Hofler
Naval Postgraduate School
Monterey, CA